SYNTHESIZING MULTIMODAL IMAGING PROBES AND THEIR APPLICATION IN NON-INVASIVE AXONAL TRACING BY MAGNETIC RESONANCE IMAGING

by

Zizhen Li

Thesis submitted to the

Faculty of Graduate and Postdoctoral Studies

in partial fulfillment of the requirements for

the Master of Applied Science degree in Chemical Engineering

uOttawa

Department of Chemical and Biological Engineering

Faculty of Engineering

University of Ottawa

ABSTRACT

Imaging techniques have become much more in demand in modern medicine, especially in fields of disease prognosis, diagnosis and therapeutics. This is because a better understanding of different diseases, characteristics of each patient and further optimizing treatment planning, are all enhanced by advanced imaging techniques. Since each imaging modality has its own merits and intrinsic limitations, combining two or more complementary imaging modalities has become an interesting research area.

In this study, gadolinium (Gd^{3+}) doped CdTe quantum dots (QDs) were synthesized and used as multimodal imaging probes of two highly complementary imaging modalities: optical imaging and magnetic resonance imaging. The new imaging probes were characterized by X-ray diffraction (XRD), transmission electron microscopy (TEM), UV-vis absorbance spectra, fluorescence spectra (FL) and magnetic resonance imaging (MRI).

The optical / MRI imaging probes were further functionalized by conjugating with the axonal tracer dextran amine (10 kDa) for non-invasive axonal tracing observations. Biocompatibility and MRI contrast effect of prepared multimodal imaging probes were investigated by in vitro cell experiments and MRI scanner. Ultimately, it is hoped that this imaging probe will help us better understand the regeneration mechanisms in real time without sacrificing animals at intervening time-points.

RÉSUMÉ

Les techniques d'imagerie sont beaucoup plus en demande dans la médecine moderne, en particulier dans les domaines du pronostic, du diagnostic et de la thérapeutique des maladies. Cela s'explique par le fait qu'une meilleure compréhension des différentes maladies, les caractéristiques de chaque patient et l'optimisation continue des plans de traitement dépendent toutes des techniques d'imagerie de pointe. Étant donné que chaque modalité d'imagerie comporte des avantages et des limites intrinsèques, la combinaison de deux modalités d'imagerie complémentaires ou plus constitue présentement un domaine de recherche intéressant.

Dans cette étude, des points quantiques de CdTe (QDs) dopés au gadolinium (Gd^{3+}) ont été synthétisés et utilisés comme les sondes d'imagerie multimodale de deux modalités d'imagerie fortement complémentaires: l'imagerie optique et l'IRM. Les nouvelles sondes d'imagerie étaient caractérisées par la diffraction des rayons x (DRX), la microscopie électronique à transmission (TEM), les spectres d'absorption UV-visible, les spectres de fluorescence (FL) et l'imagerie par résonance magnétique (IRM).

Des sondes optiques/d'imagerie IRM ont été encore plus fonctionnalisées en les conjuguant avec un traceur axonal de dextran aminé (10 kDa) pour observer le tracé axonal de manière non invasive. Par la suite, la biocompatibilité et l'effet de contraste en IRM des sondes d'imagerie multimodales préparées ont fait l'objet d'une analyse

premièrement au moyen d’une expérience cellulaire in vitro puis d’un scanner IRM. En fin de compte, il faut espérer que cette sonde d’imagerie nous aidera à mieux comprendre les mécanismes de régénération en temps réel sans sacrifier des animaux entre-temps.

ACKNOWLEDGEMENTS

I would first like to acknowledge my supervisor, Prof. Xudong Cao, for his guidance, support, and mentorship during my master studies, as well as providing me a research assistant position while I pursue my degree of Master of Applied Science.

I would also like to acknowledge the Natural Science and Engineering Research Council of Canada (NSERC) and Canadian Institutes of Health Research (CIHR) for financially supporting this project, and the Faculty of Graduate and Postdoctoral Studies (FGPS) by providing me the Admission Scholarship.

I am also grateful to technicians at the Center for Catalysis Research and Innovation (CCRI) at the University of Ottawa and National Research Council (NRC): Dr. Tara Kell (X-ray diffraction, Dept. Earth Sciences), Dr. Yun Liu (transmission electron microscopy, CCRI), Dr. Jianying Ouyang (fluorescence spectra, NRC) and Dr. Xiangyang Liu (fluorescence spectra, NRC). And I would also like to thank the technical officers, especially Louis Tremblay in the department of Chemical and Biological Engineering.

I would like to acknowledge the work of undergraduate student who participate in this project, Ali Dergham. I also want to extend my thanks to all of my colleges during my graduate studies, especially Yan, Chunyu, Yuqian, Yubo, Jian, and Taisa.

Finally, I would like to thank my warm family, the selfless help of my parents and my

beloved boyfriend (Xiangchao Meng). Without whom, none of this would have been possible.

TABLE OF CONTENTS

LIST OF FIGURES

LIST OF TABLES

ABBREVIATIONS

Abbreviations	Name
BDA	Biotinylated dextran amine
CB	Conduction band
CNS	Central nervous system
DA	Dextran amine
dCSF-CNs	Distal cerebrospinal fluid-contacting neurons
DiI	1,1'-dioctadecyl-3,3,3'3'-tetramethylindocarbocyanine perchlorate
DOTA	1,4,7,10-tetraazacyclododecane-1,4,7,10-teraacetic acid
DY	Diamidino Yellow
EDC	1-ethyl-3-(3-dimethylaminopropyl)carbodiimide hydrochloride
EDS	Energy dispersive x-ray analysis
EM	Electron microscopic
FB	Fast Blue
FBS	Fetal bovine serum
GSH	Glutathione
HMP	Hexametaphosphate
HRP	Horseradish peroxidase
HRTEM	High resolution transmission electron microscopy
LED	Light-emitting diode
LM	Light microscopic
MRI	Magnetic resonance imaging
MTT	Methyl thiazolyl tetrazolium
NHS	N-hydroxysuccinimide
PBS	Phosphate buffered saline
PET	Positron emission tomography

QD	Quantum dot
Abbreviations	**Name**
QY	Quantum yield
R6G	Rhodamine 6G
RGD	Arginine-glycine-aspartic acid
RSH	3-mercapto-1, 2-propane-diol
TEM	Transmission electron microscopy
TGA	Thioglycolic acid
TOP	Trioctylphosphine
TOPO	Trioctylphosphine oxide
VB	Valence band
VEGF	Vascular endothelial growth factor
VEGFR	Vascular endothelial growth factor receptors
XRD	X-ray diffraction

CHAPTER 1

INTRODUCTION

1.1 Introduction

Imaging technologies, such as MRI, optical imaging and ultrasound imaging, have become much more significant in modern medicine, especially in fields of disease prognosis, diagnosis and therapeutics. However, the intrinsic limitations associated with each imaging modality hinders their potential applications, making it a challenge to choose a well-suited imaging modality for target disease [1]. To solve this problem, the revolutionary concept of integrating two or more complementary imaging modalities has triggered a significant amount of attention in studies on multimodal imaging probes [2]. To date, the commercialized PET/CT and PET/MRI instruments have been adopted clinically [3], and more merged instruments and multimodal imaging probes are on the way [4-6]. This trend facilitates a blooming development of multimodal imaging probes design.

Generally speaking, the design of multimodal imaging probes starts from rationally selecting appropriate imaging modalities based on the final purpose and complementarity of selected imaging modalities. This is followed by integrating corresponding imaging agents, usually by either encapsulation, doping, or bioconjugation. In this work, our objective is to accomplish non-invasive axonal tracing to better assess the state of nerve regeneration in real time, and better design nerve regeneration strategies. Non-invasive means our imaging probes do not need to destroy healthy tissue and are not limited for penetration depth. MRI is considered superior for central nervous system (CNS) imagig

ng due to its demonstrated good tissue contrast, non-invasive imaging ability and unlimited tissue penetration [7-9]. Therefore, MRI is widely used in studies correlated with CNS, such as tracing molecules in brain and spine [10], monitoring inflammatory cellular activity in brain [11] and displaying features of primary central nervous system lymphomas [12]. The relatively low sensitivity and lack of resolution at the cellular level, however, are the limitations of the MRI modality. In contrast, optical imaging has high sensitivity and ability to provide detailed biological information at the cellular or subcellular levels [3, 13]. Therefore, combining these highly complementary imaging modalities could accomplish non-invasive axonal tracing associated with precise anatomical and physiological information.

In comparison with conventional fluorophores (*e.g.* lanthanide chelates, organic dyes and fluorescent proteins) [14], semiconductor nanocrystals (QDs) have many unique optical properties including broad absorption spectra, tunable emission wavelength, good resistance to metabolic degradation as well as high photostability [15]. In addition, they are easy to be functionalized due to the existence of large amount of ligands on the surface. As a result, QDs have been used as a versatile fluorescent probes in various areas, such as targeted deliveries (e.g. siRNA delivery) [16, 17], multiplexed biological applications (e.g. multiplexed detection of protein sequences) [18], and optoelectronic devices (e.g. LED and photodiodes) [19, 20], and offers a promising platform to combine optical imaging with MRI, if the QDs can be magnetized.

Currently, there are four major synthetic methods to prepare magnetic QDs [3]: (1) attaching magnetic chelates on the QDs surface [21]; (2) co-encapsulating QDs and magnetic particles [22], (3) growth a heterocrystalline structure [23], and (4) doping paramagnetic ions within QDs [24]. Among all methods, QDs produced by doping paramagnetic ions generates smaller products. Small sizes are beneficial to cell uptake in order to increase the imaging sensitivity and reduce the toxicity associated with imaging probes. Moreover, small sized particles are known to have accelerated excretion rate from our body, which also reduces the risk caused by imaging probes

[25]. In addition, most paramagnetic ion-doped QDs are prepared by one-step synthetic methods [26-28]. The simple synthesis method increases the reproducibility and makes their products easy to be commercialized. Therefore in this study, QDs (CdTe) were prepared as fluorescent probes, and doped by gadolinium (Gd^{3+}) with the goal of producing novel optical/MRI multimodal imaging probes (CdTe:Gd QDs) .

Nerve system consists of central nervous system (CNS) and peripheral nervous system. In peripheral nervous system, nerves have capacity for regrowth due to the facilitation of some cytokines [29] and the regeneration rate is about 2-5 mm/day [30]. Unfortunately, CNS axons lack of regrowth ability due to the inhibition of several glycoproteins [31-33] and the formation of glial scars [34]. However, synthetic scaffold provides a promising therapy for CNS axons regeneration [35]. In the studies related to nerve or neural tissue repair, neuronal tracing techniques are widely used to monitor the state of regenerated neurons [36, 37]. However, currently used neuronal tracers such as dextran amine conjugates [38, 39], fluoro-gold [40, 41], as well as 1,1'-dioctadecyl-3,3,3'3'-tetramethylindocarbocyanine perchlorate (DiI) [42, 43] do not offer non-invasive visualization. The lack of reliable non-invasive techniques to monitor the state of nerve regeneration over time has been considered as a factor resulting in the failure of some clinical trials [44]. For example, in neuroma treatment, lack of reliable techniques to explore the state of nerve injury or repaired nerves is considered to mislead the surgeon to do unnecessary operation to evaluate whether sufficient regeneration is occurred or not [45]. On the other hand, insufficient evidence makes the surgeon miss the good timing for operation [46].

To accomplish the non-invasive axonal tracing effect, CdTe:Gd QDs were conjugated with dextran amine (DA, 10 kDa). Dextrans with low molecular weight (3 kDa) are preferred for transporting in the retrograde direction and for labeling neuronal cell bodies. Dextrans with higher molecular weights (≥10 kDa) yield exquisitely detailed labelling of axons and terminals. Ten kDa dextrans have better transport efficiency than higher weight forms [47].

In summary, there is an immediate need for non-invasive neuronal tracing for pre-clinical and clinical studies. Therefore, the focus of this thesis is to develop a novel multimodal imaging probe, DA-CdTe:Gd QD, that can be detected non-invasively by both MRI and optical imaging techniques.

1.2 Objectives

The objectives of this project are as follows:

- Prepare CdTe:Gd QDs optical/MRI multimodal imaging probes and optimize the synthesis conditions, including pH and Gd / Te molar ratio
- Characterize the as-prepared CdTe:Gd QDs under optimal synthesis conditions with X-ray diffraction (XRD), transmission electron microscopy (TEM), UV-Vis absorbance spectra, fluorescence spectrum and magnetic resonance imaging

(MRI)

- ❖ Surface functionalize the CdTe:Gd QDs by conjugating DA molecules on the surface to acquire axonal tracing properties, and explore the effect of varying initial DA to CdTe:Gd QDs molar ratios on the final amount of conjugated DA molecules;
- ❖ Investigate the biocompatibility and MRI contrast effect of prepared DA-CdTe:Gd QDs

1.3 Thesis structure

The main body of this thesis includes five chapters: introduction, background and literature review, experimental, results and discussions and conclusions and future work. Detailed description of each chapter is shown below:

- ❖ Chapter 1: Introduction

Relevant background information, significance, objectives and structure of the project have been introduced.

- ❖ Chapter 2: Background and literature review

A general literature survey and significance related to this project are discussed.

- ❖ Chapter 3: Experimental

Synthesis procedure and characterization methods of CdTe:Gd QDs are described. Furthermore, DA conjugation procedure and cytotoxicity evaluation of DA modified CdTe:Gd QDs is introduced.

- Chapter 4: Results and Discussion

Optimal synthesis conditions of CdTe:Gd QDs have been determined and the as-prepared CdTe:Gd QDs under optimal synthesis conditions are characterized. The relationship between initial DA to CdTe:Gd QDs molar ratio and final amount of conjugated DA molecules per QDs have been reported. The cytotoxicity and MRI contrast effect of DA-CdTe:Gd QDs are evaluated.

- Conclusions and Future Work

Conclusions and some recommended future work are described.

CHAPTER 2

BACKGROUND AND LITERATURE REVIEW

2.1 Quantum dots

Quantum dots (QDs) are semiconductor nanocrystals, ranging in diameters between 1-10 nm, containing roughly 200-10,000 atoms [48]. Since the first synthesis of QDs three decades ago, their attractive intrinsic properties of the QDs have motivated increasing research efforts on their applications in optoelectronic devices [49], bio-imaging [50], labeling techniques [51] and sensing [52]. These attractive properties include size-dependent electrical and optical properties. In the early 1980's, these unique properties were first reported by Ekimov and Efros [53-55] via a theoretical framework based on the quantum confinement effect. This pioneering works drove research to explore the field of QDs. In 1986, Reed *et al.* first proved the fully quantized crystalline structure of QDs and created the word "quantum dot" to describe the systems in which electrons are restricted in all three dimensions [56]. After a decade, the Nie [57] and Alivisatos groups [58] almost simultaneously accomplished fabrication of water-soluble QDs and capping QDs with biomolecules to make them functional optical probes. These groundbreaking studies highlighted the potentials of QDs in the biomedical field, especially in biomedical imaging. Water-soluble QDs feature unique optical properties; this make them one of the most promising fluorescent probes. To date, advanced optical properties of QDs have been widely utilized in intracellular single particle tracking, cell labeling, cancer diagnosis and therapeutics, in vivo molecular imaging, and drug delivery [51, 59-63].

2.1.1 QDs Fluorescence Mechanism

The existence of a band gap between the valence band and conduction band is an important feature of semiconductors. Once a semiconductor is activated by a photon with an energy larger than band gap energy (E_g), an electron (e) can be excited above the valence band energy to the conduction band leaving a hole (h) in the valence band. These opposite charges can bond by Coulombic attraction, and form an electron-hole pair (e-h), which is also known as an exciton. The interaction between e-h pairs is weak and the recombination of the e-h pairs can release energy in the form of a photon, which is called radiative recombination.

Interestingly, the situation is different when the physical size of the bulk semiconductor is reduced to a critical size, called the Bohr exciton diameter. The continuous energy gap of a bulk semiconductor becomes discrete, similar to the discrete energy levels of electrons in an atom. As a result, QDs are also known as artificial atoms. Secondly, the band gap energy increases with the reduction of the particle radius (R). The band gap energy is roughly proportional to $1/R^2$ [64]. For this reason, there is a blue shift of the absorption and corresponding emission wavelengths that correlates with a reduction in QD size. These differences are caused by the quantum-size effect [64]. Schematics of the electronic energy states of bulk crystal and QDs are shown in Figure 1.

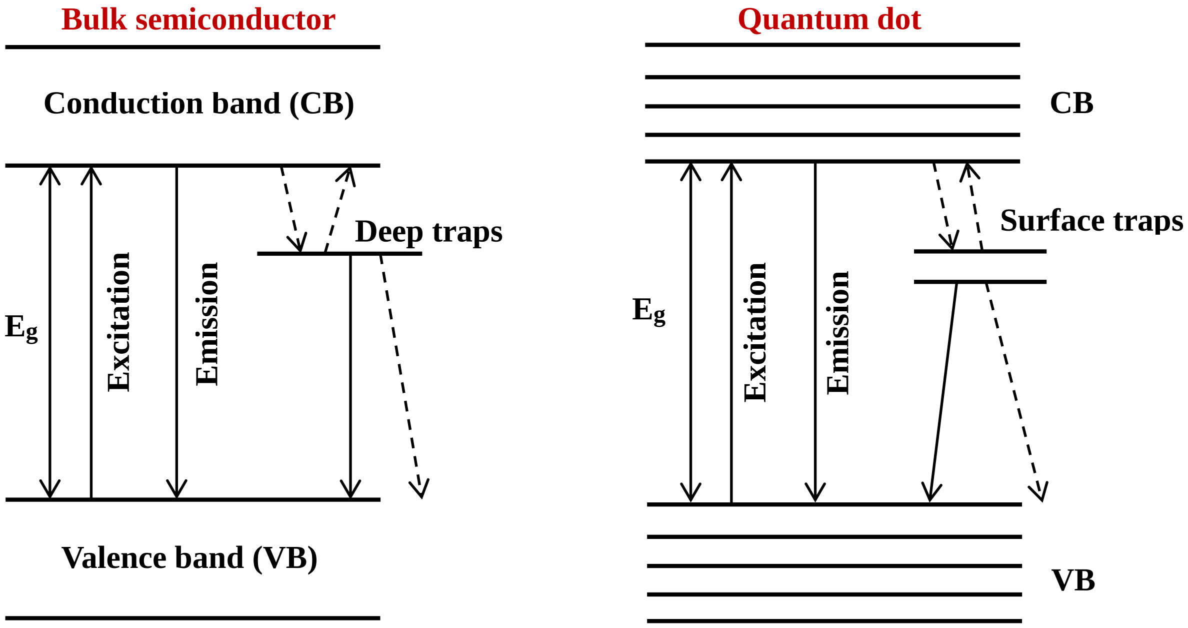

Figure 1. Electronic energy states of bulk crystal and QDs (reproduced from [65]).

2.1.2 Optical Properties of QDs

The optical properties of QDs are determined by their composition, size and surface states that are influenced by the number of dangling bonds on the surface that result in nonradioactive recombination [66]. As a consequence of their numerous unique optical properties, QDs have become a prominent fluorescent material compared with conventional fluorophores [14, 15]. The optical properties of QDs are summarized below.

2.1.2.1 Broad and continuous absorption spectra

QDs with broad absorption spectra, can be excited by a wide range of wavelengths which are shorter than the wavelength of first exciton absorption peak. While organic dyes such as fluorophores can only be excited by a range of wavelengths above and below specific wavelength (Figure 2 (A)). Therefore, multiply colored QDs can be excited simultaneously by the same excitation wavelength. This can dramatically simplify the instrument used for multiplexed detection [18].

A

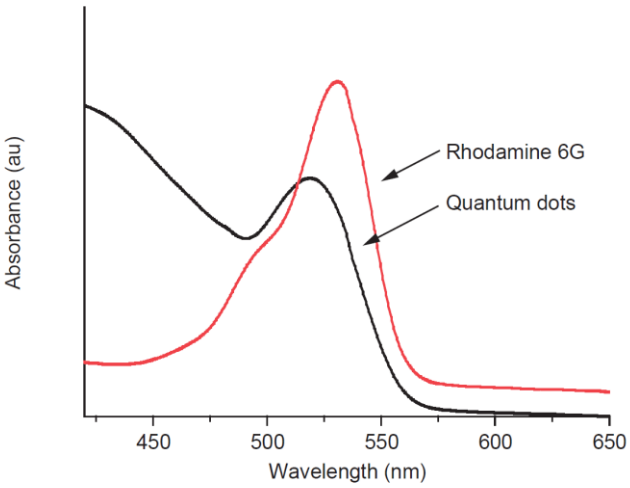

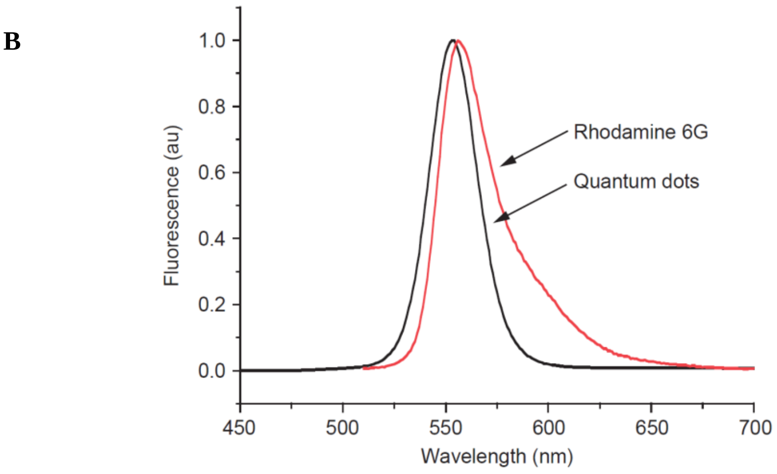

Figure 2. Absorption (A) and emission (B) spectra of rhodamine 6G and CdSe QDs (reprinted from Ref. [67] with permission from Elsevier).

2.1.2.2 Narrow and symmetric emission spectra

Compared with fluorescent dyes, QDs have a narrower and symmetric emission profile (Figure 2 (B)) than the fluorophores, which can effectively eliminate the signal interference caused by spectral overlap and 'red tails'. Therefore, QDs with different emission wavelengths can tag different molecules allowing for simultaneous distinction of differently tagged molecules, with high detection sensitivity. For instance, Nie *et al*. group that 6 colored QDs with 10 intensity levels could encode 1,000,000 nucleic acid or protein sequences [68].

2.1.2.3 QD Stability

Organic dyes are limited by poor photostability [69-71] and thermal instability [72] which hamper their applications in long-term imaging, and reduce detection sensitivity under intense excitation. In contrast, QDs are resistant to metabolic degradation or photobleaching owing to their inorganic composition, and adequately passivated surface by shell or capping ligands. This extraordinary advantage of QDs has been discussed in the literature [73-75]. QDs stabilities up to 100 times higher than that of commonly used organic fluorescent dyes [57].

2.1.3 QD Synthesis Methods

2.1.3.1 Development of an aqueous synthesis method

The synthesis method plays an important role in controlling the properties of prepared QDs, and their applications. The most widely used strategies for QD preparation are the organometallic and the aqueous synthesis methods. The organometallic method employs high-boiling-point and toxic solvents (*e.g.* trioctylphosphine or trioctylphosphine oxide (TOP or TOPO)) [76-78], and in general the QDs lack the intrinsic aqueous solubility [78] which hinders their biological applications. In contrast, the aqueous fabrication method has the following advantages: (a) it uses water, the most environmentally-friendly solvent (b) it is simple and offers high reproducibility; (c) it is easily scalable; (d) it can be performed in ambient conditions, and (e) it provides versatile applications by using appropriate capping ligands to be further linked with other biomolecules. Thus QD preparation with the aqueous synthesis method has become a promising alternative to the conventional organometallic fabrication method.

In 1993, Nozik *et al.* [79] first synthesized QDs in aqueous solutions . In their report, 3- mercapto-1, 2-propanediol capped CdTe QDs were synthesized with $CdSO_4$ and NaHTe as Cd^{2+} and Te^{2-} sources. To stabilize the QDs in the aqueous solution, hexametaphosphate (HMP) and 3-mercapto-1, 2-propane-diol (RSH) were used as stabilizers. After this milestone work, subsequent efforts were reported by Weller's [80, 81] and Rogach's [82] groups that reported various effects that thiol stabilizers had on QDs. Since then, a variety of short-chain thiol stabilizers provide desired surface groups such as -COOH, $-NH_2$, and -OH were studied. The most commonly used thiols are shown in Figure 3 [82]. Zhou *et al.* [83] recently utilized a conical flask as the only reaction equipment required to synthesize CdTe QDs, which significantly simplified the previous aqueous synthesis methods. In their experiment, no pretreatments such as N_2 protection, pH adjustment or Te precursor preparation were required. Sequential addition of water, $CdCl_2$, thiol stabilizer, Na_2TeO_3, $NaBH_4$, and $N_2H_4•H_2O$ produces QDs. The particle size was controlled by altering the molar ratio of reagents. While promising, this synthesis method is potentially limited by the use of a large amount of toxic and less biocompatible hydrazine monohydrate ($N_2H_4•H_2O$).

In the following sections, several aqueous synthesis methods of CdTe QDs are presented in detail.

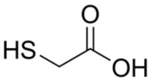

Thioglycolic acid

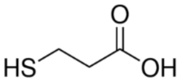

3-mercaptopropionic acid

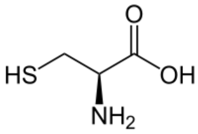

L-cysteine

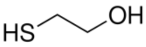

2-mercaptoethanol

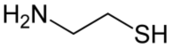

Cysteamine

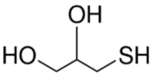

1-thioglycerol

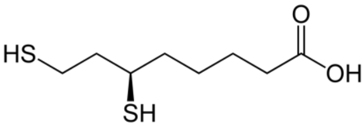

Dihydrolipoic acid

2-(dimethylamino)ethanethiol

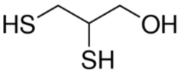

2, 3-dimercapto-1-propanol

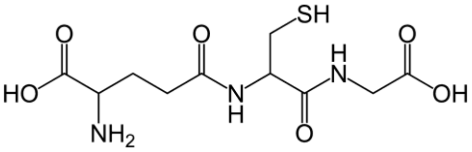

Glutathione (GSH)

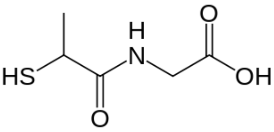

Tiopronin

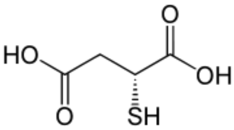

Mercaptosuccinic acid

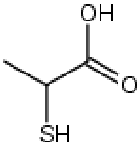

2- mercaptopropionic acid

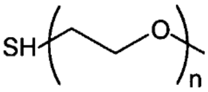

mPEG- SH (n=7-16)

Figure 3. Most commonly used thiols (reprinted from Ref. [82] with permission from Royal Society of Chemistry Publisher).

2.1.3.2 Refluxing method

In a conventional aqueous refluxing procedure, cadmium salt is dissolved in water containing an appropriate stabilizer, usually a thiol, followed by the injection of a Te precursor. The Te precursor is prepared by reducing Te powder by $NaBH_4$ [84] or chemical decomposition of Al_2Te_3 upon inert gas protection [85]. Subsequently, nucleation and crystal growth are initiated by heating and refluxing. Note that the size of QDs increases gradually with an increase of refluxing time.

In comparison with the organometallic route, QDs synthesized by the conventional aqueous refluxing process have aqueous solubility that is useful for bioapplications. However, the conventional refluxing route still has some drawbacks, such as a relatively low growth rate at 100 ℃, use of unstable Te precursors (NaHTe or H_2Te) which could oxidize easily and complicated multistep process steps, especially the Te source injection, may vary between operators. As a result, a series of systematic studies have been carried out to improve this method during the past two decades, and the improved method is referred to as the aqueous refluxing method.

Zou *et al.* [86] have made a significant improvement in changing the time-consuming conventional refluxing process by increasing the pH of the reaction mixture to greater than 11.5 and reducing the Te to Cd molar ratio to less than 1:10. These changes resulted in a CdTe QD growth rate increase of approximately 100 times. CdTe QDs with emission wavelengths from 542 nm to 807 nm required 90 min while the quantum yields (QYs) were as high as 50%. The QYs of near- infrared QDs reached 25%. These were the best QDs production results with the aqueous method at that time.

In order to simplify the synthesis process and avoid the use of unstable Te precursors, the “one-step” or “one-pot” refluxing method was introduced by Sheng *et al.* [87]. In their article, Na_2TeO_3 was used as a Te precursor and glutathione (GSH) was stabilizer. CdTe QDs with emission wavelengths from 520 nm to 625 nm in 1.5 h of refluxing were obtained. The QDs showed relatively low cytotoxicity and high QYs (84%). Subsequently, the one-step synthesis of doped QDs was reported. Qisui *et al.* [88] reported a one-step growth of CdTe QDs doped with Zn^{2+} with QYs up to 72%. Figure 4 shows the difference between the conventional refluxing equipment and a one-step refluxing method with GSH as a stabilizer.

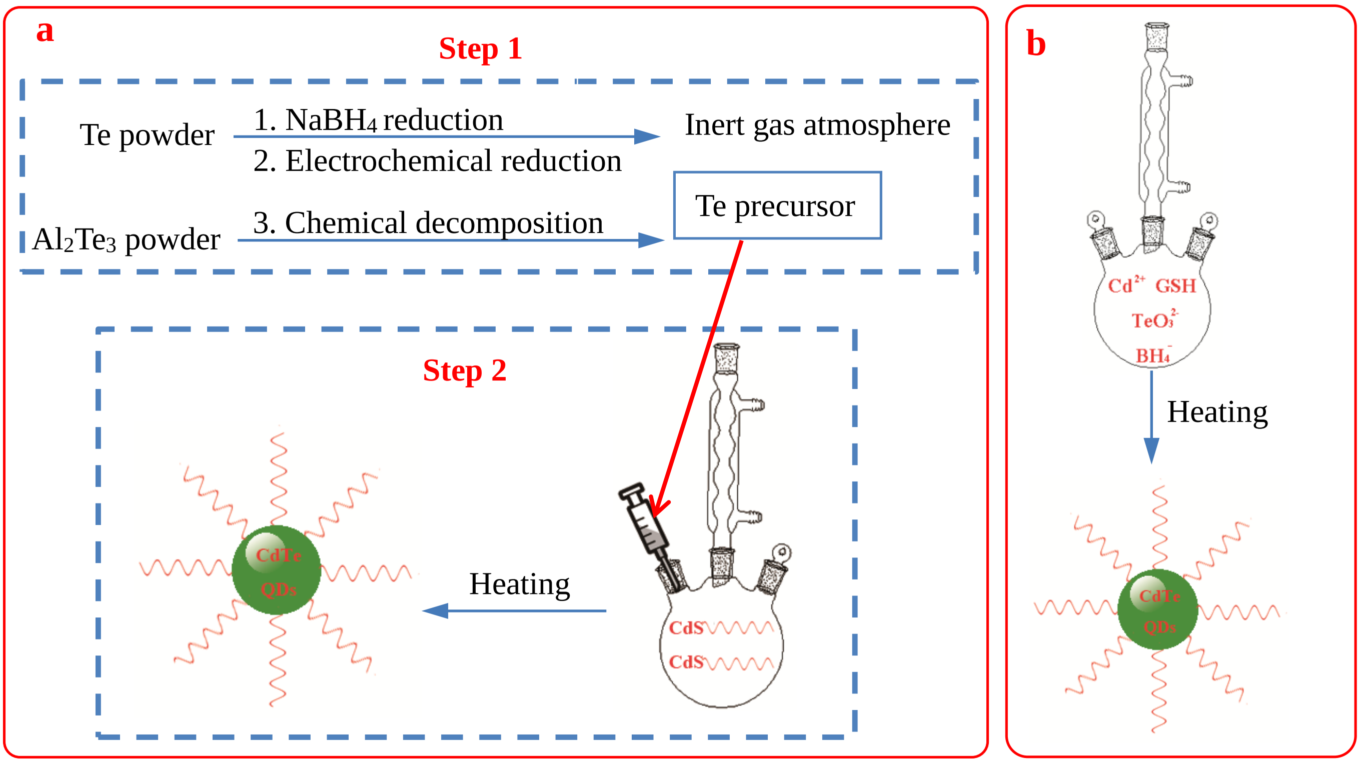

Figure 4. Schematic of the conventional refluxing method (a) and one-step refluxing method with GSH as a stabilizer (b) (reproduced from Ref. [87] with permission from the Royal Society of Chemistry).

2.1.3.3 Hydrothermal method

Compared with refluxing method, hydrothermal method can produce QDs with better monodispersion [89]. In the hydrothermal method, all reactions take place in an autoclave under high pressure and high temperature in the presence of water as a solvent. In 2003, Zhang *et al.* [89] first use the hydrothermal method to synthesize aqueous QDs. In their experiment, previously prepared CdTe precursors were transferred into a Teflon-lined autoclave and then heated to 160~180 ℃ to accelerate the growth rate of

CdTe QDs. Low precursor concentration resulted in a higher QY of the green-yellow emission which was attributed to excess cadmium monomers that were favored for surface reconstruction and ordering. When the Cd precursor concentration was 1.25 mM, the molar ratio of Cd / Te / TGA (Thioglycolic acid) was 1: 0.2: 2.4, the pH was 9.0 and the reaction temperature was 180 ℃, the QY was greater than 30%, and the emission wavelength was 550 nm. On the basis of Zhang's work, Guo *et al.* [90] systematically studied the effect of TGA to cadmium molar ratio, the cadmium to tellurium molar ratio, and reaction temperature on CdTe QDs synthesis. According to their results, the QY was strongly dependent on the molar ratio of TGA/Gd. An increased TGA to cadmium molar ratio decreased the QY, changing it from 40.8% to 3% when the TGA to cadmium molar ratio was 1.2 or 4.8.

Although CdTe QDs prepared by the hydrothermal method have an improved crystalline structure and narrower size distribution, the use of this method has been limited because of its poor scalability due to special equipment requirements, such as high temperature and pressure.

2.1.3.4 Microwave-assisted aqueous synthesis method

Microwave irradiation, which involves electromagnetic waves with frequencies ranging from 300 MHz to 300 GHz, has been widely used in chemical catalysis, nanomaterials synthesis and organic reactions as an assisted heating method [91]. The microwave-assisted heating method has three advantages: (a) a small thermal gradient because of homogeneous heating, (b) selective heating due to the different dipole constants of different of substances, and (c) high utilization efficiency of microwave energy leading to a rapid heating. On account of these advantages, the microwave-assisted heating method was first applied to aqueous QDs synthesis in 2005 [91]. In this protocol, a CdTe precursor was prepared by mixing $CdCl_2$, NaHTe and MPA in water. The reaction mixture was put into a vessel and microwaved. By optimizing the reaction time and temperature, a series of different-sized CdTe QDs were obtained. To date, the microwave-assisted aqueous synthesis method has been used to synthesize CdSe [92] and ZnSe [93] QDs, and core/shell QDs such as CdTe/CdS [94], CdTe/CdS/ZnS [95] and CdSe/ZnS [96] QDs.

2.1.3.5 Biosynthesis method

This method is considered the most environmentally-friendly approach and has attracted increasing attention in recent years. A study published by Bao *et al.* [97] used yeast cells as a matrix to synthesize size-tunable CdTe QDs under a relatively mild condition (25~35 ℃). Their approach consists of two pathways: an extracellular growth pathway and an endocytosis pathway (Figure 5), accomplished by adding inorganic metal precursors to yeast cell culture media. The emission wavelength of as-prepared CdTe QDs was reported between 490 nm to 560 nm due to the tunable size from 2.0 nm to 3.6 nm. In addition to the good optical properties, these biosynthetically prepared QDs were protein-capped and could be further functionalized if needed. It should be noted that QDs synthesized using living organisms not only are considered 'green', but also show excellent biocompatibility and lower cytotoxicity [97].

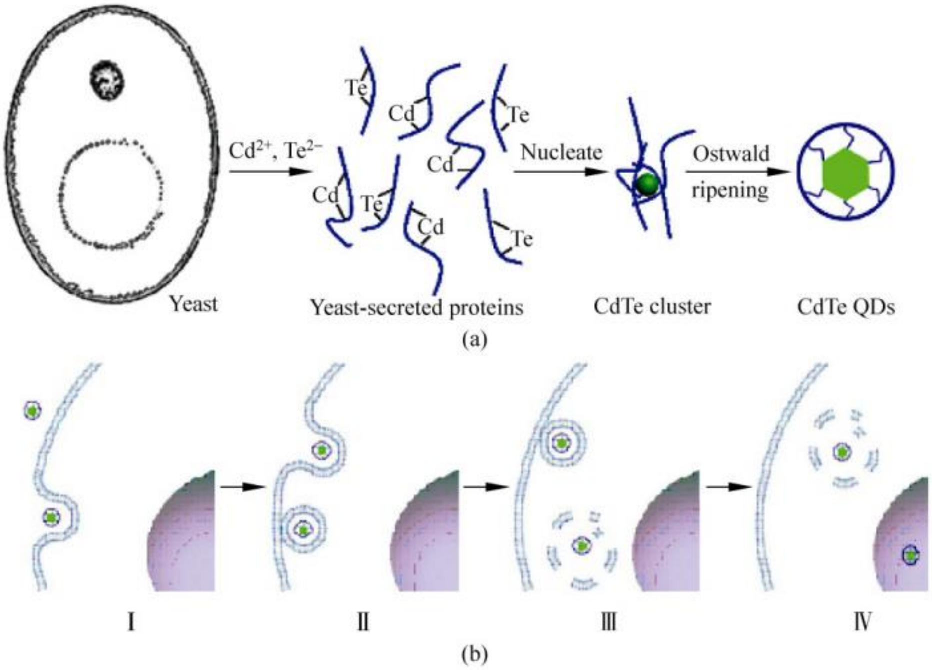

Figure 5. Schematic of the biosynthesis method: (a) extracellular growth pathway and (b) endocytosis pathway. (reprinted from Ref. [97] with permission from Springer Publisher).

2.2 Applications of QDs

2.2.1 QDs-based Multimodal Imaging Probes

2.2.1.1 Multimodal imaging and multimodal imaging probes

Disease prognosis, diagnosis and even further treatment plans all rely on advanced imaging [98]. However, each imaging modality has its limitations, which hinder its full potential in clinical applications [1]. Advantages and limitations of frequently used imaging modalities are summarized in Figure 6. To acquire more precise biological information about the disease, two or more imaging modalities are used, which increases diagnosis time. Also, the side-effects caused by multiple dosages of agents is harmful to the patient [99].

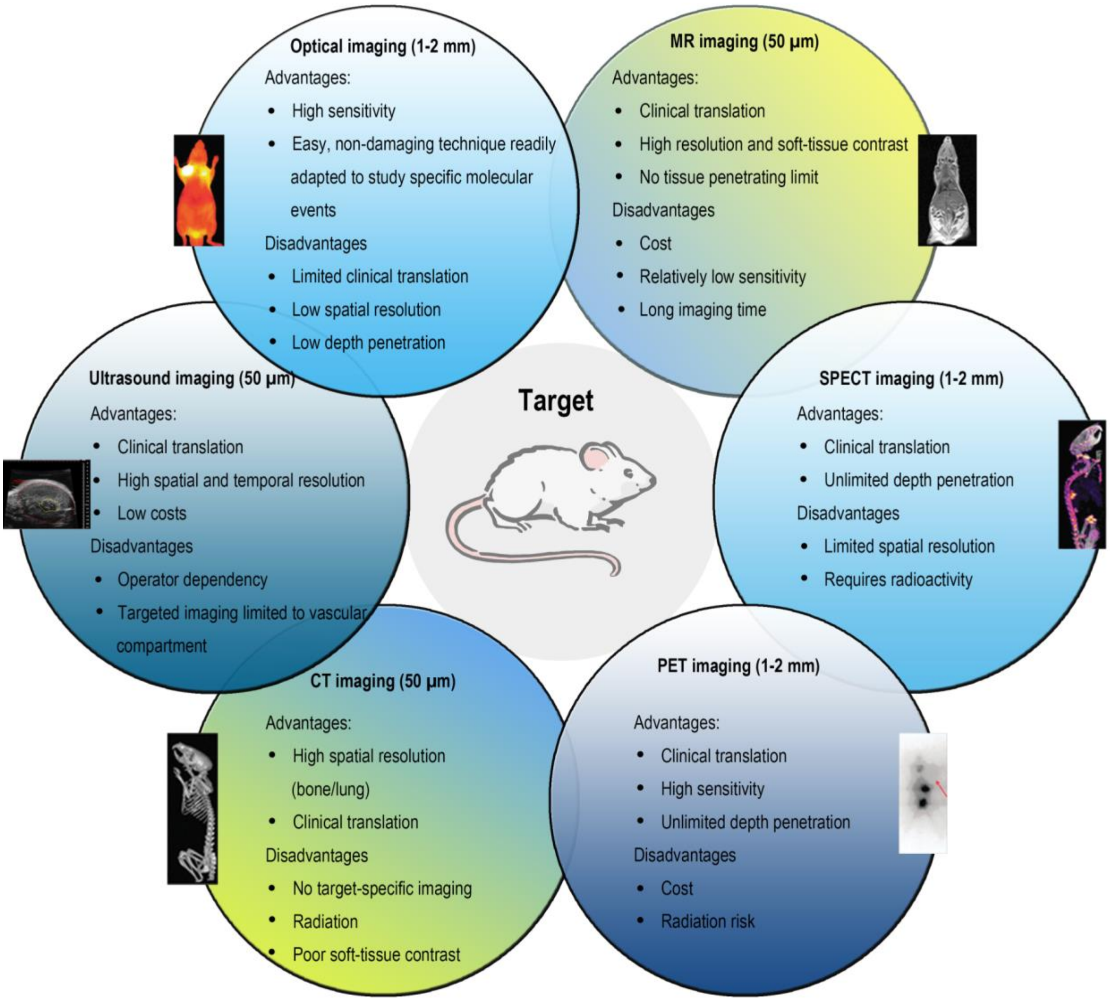

Figure 6. Advantages and limitations of frequently used imaging modalities (Reproduced from Ref. [98] with permission from the Royal Society of Chemistry).

To solve above problems, the idea of integrating two or more complementary imaging modalities has triggered a sharp rise in the manufacture of hybrid medical equipment and studies related to multimodal imaging probes design [2]. Since the first appearance of merged PET/CT instrument in 1998 by Townsend and colleagues [100], the market of multimodal imaging probes has been expanded rapidly to include products such as liposome-encapsulated probes [101, 102], dendrimers-coupled probes [103, 104], iron oxide nanoparticle-based probes [105-107], silica-based nanoparticles [108-110], QDs-based probes [111-113]. Among them, QDs become competitive optical probes due to their unique optical properties and abilities to be integrated with other imaging modalities to form hybrid imaging probes.

2.2.1.2 QDs-based optical/MRI multimodal imaging probe

MRI and optical imaging modalities are a nearly ‘perfect’ match for each other. Optical imaging has high sensitivity and the ability to image at cellular and even subcellular levels but suffers from low tissue penetration and spatial resolution [114]. In contrast, MRI has unlimited depth penetration and high spatial resolution; however, it lacks sufficient sensitivity and visualization at the cellular level [4, 98]. It is possible to combine these two modalities together, and generate more detailed anatomic information and precise imaging of target tissues, such as optical/MRI imaging probes for target tumor imaging [17]. Due to the highly complementary properties between optical and MRI imaging modalities, QDs-based optical/MRI dual imaging probes have been intensely researched recently [115-118].

A commonly used model of optical/MRI dual imaging probes consist of Gd-lipids and QDs that are prepared by coating the QD surface with a layer of Gd chelates as shown in Figure 7 [119]. This micelle structure is also widely used as a typical structure of QD used in neuroscience [120, 121]. The synthesis process of these construct involves self-assembly of amphiphile (*e.g.* PEG-lipids), inserting paramagnetic bonded lipid (*e.g.* Gd-lipids), and further functionalizing the resulting lipid with biomolecules (*e.g.* RGD peptide). However, this method has low reproducibility and yield because the process of linking a new type of ligand usually results in detachment of previously attached ligands. This is because both covalent bonds and secondary hydrophobic or hydrophilic interactions are sensitive to temperature, pH, solvents and other factors [122]. Additionally, attaching multiple ligands leads to complicated synthesis procedures, especially when attaching more than two ligands simultaneously. In comparison with the conventional optical/MRI multimodal imaging probe [119], Gd doped QDs or enrolling Gd ions as a component of a QD matrix is a promising approach to use optical imaging and MRI together with one probe [17, 123].

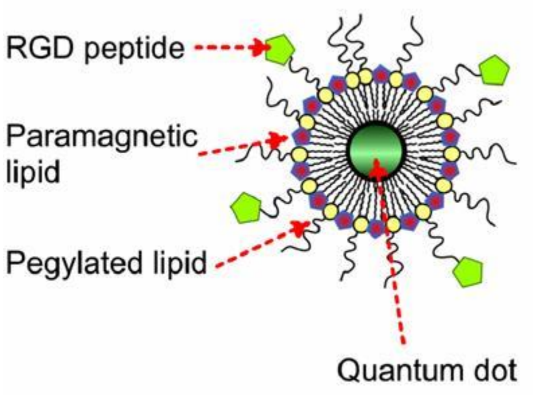

Figure 7. Schematic drawing of a quantum dot (QD) (green) encapsulated in PEG-lipids (red) and paramagnetic (yellow) lipids. A small fraction of the paramagnetic lipids was functionalized by an arginine-glycine-aspartic acid (RGD) peptide, which enables targeting to a cell surface receptor (reprinted from Ref. [119] with permission from the American Chemical Society).

2.2.2 QDs Applications in Cancer Therapy and Neuroscience

Due to their strong fluorescence intensity, good photostability and easy to be functionalized, QDs have entered neuroscience and cancer therapy area for target delivery, and tracking, labeling, and visualizing cellular events recently [120, 124, 125]. Evelyn *et al*. applied QDs to track the metastasis of tumor cells in vivo by fluorescence emission-scanning microscopy [126]. They found QDs are well-suited to visualize single cells and track tumor cell extravasation in living animals because QDs have no detectable effect on the behavior of labeled tumor cells and host animal. In addition, QDs with different emission wavelength can examine the multicellular interactions simultaneously. Because folate receptors are expressed on the surface of a variety of cancers, folate-QDs conjugates are widely used as therapeutic carriers or targeted fluorescent probes in cancer diagnosis or therapy [125].

QDs are also widely used in neuroscience [120, 124]. A study by Michael *et al.* combined QDs with gradient index (GRIN) lenses to visualize in vivo deep tissue. Their research provides a new approach for microangiography in deep brain tissue with high penetration depth up to 2 mm. Robert *et al* measured brain extracellular space via the in vivo diffusion of QDs [127]. A representative width of 38-64 nm was reported based on their results, which is more than 2 times larger than the width measured from a fixed tissue. Therefore, they suggested the size limit of a drug delivery vector is 64 nm for uniform and effective diffusion in most of brain tissue. Maxime and coworkers used glycine functionalized QDs to track the lateral mobility of glycine receptors in living neurons for 20 min [128]. Their study indicates that QDs are allowed for tracing dynamic cellular processes with high sensitivity.

All the studies above demonstrate that QDs are promising tools in various research areas owing for the unique semiconductor fluorescence property and special physiochemical properties.

2.3 Neuronal tracers

Since Kristensson and Olsson successfully deposited the enzyme horseradish peroxidase (HRP) as tracer into rats in 1971 [129, 130], neuronal tracers have been widely studied. To date, commonly used neuronal tracers include HRP, fluorescent substances, biotinylated dextran amine (BDA), viruses, and plant lectins.

The enzyme horseradish peroxidase (HRP) was identified in the roots of the horseradish plant. It is applied in organic synthesis and biotransformation reactions[131]. It has been successfully developed for use in early neuron tracing, and has been combined with light microscopic (LM) and electron microscopic (EM) techniques [132]. However, the limitations of HRP used as a neuronal tracer includes slow delivery speed, impermanent labelling, instability [131].

While HRP is widely used in the field of neuron tracing, fluorescent dyes are also used. Evans Blue, a fluorescent dye was injected into the gastrocnemius muscle of rats. A fluorescence signal was later in spinal motoneurons, indicating the feasibility of using fluorescent substances as neuronal tracers [133]. Compared with HRP, the most outstanding property of fluorescent dyes is the immediate visualization of labelled neurons by fluorescence microscopy, instead of requiring histochemistry post treatment for HRP labeled neurons. To date, a variety of fluorescents tracers have been reported, including Fast Blue (FB) [134], Fluoro-Gold (FG) [135], Bisbenzimide [136], propidium iodide [137], Granular Blue [138], True Blue [138], DAPI-primuline [139], Nuclear Yellow [140] , and Diamidino Yellow (DY) [141]. Benjamin summaried properties of the most used fluorescent tracers [142]. The disadvantages of the fluorescent tracers applied in neuron tracing are rapid fading which makes the result collection difficult [143], as well as the detailed mapping of neuronal projection systems [39].

Alternatively, dextran amine, used as biotinylated dextran amine or with fluorescent dextran, is regarded as an alternative approach for permanent labelling and detailed mapping of axons and terminals. It is a sensitive tracer to label both anterograde and retrograde pathways, depending on the molecular weight and pH of the delivery vehicle. Dextran amine (10k) tend to sensitively and exquisitely mark details of axons and terminals, while dextran amine (3k) yields sensitive retrograde labelling of neuronal cell bodies. Dextran amines are visualized by either light microscopy (LM) or electron microscopy (EM), and could be integrated with other neuronal tracing methods. Detailed protocols were comprehensively summarized elsewhere [144].

Dextran amine is transported within neurons through an inherent flow of axoplasm which is also known as axonal flow. This continual intracellular flow was first reported by Paul Weiss in 1948 [145] and enables bidirectional transport of macromolecules within neurons. Therefore, dextran amines with different molecular weights are transported anterogradely or retrogradely. The uptake mechanism of dextran amines appears to be endocytosis by intact neurons [146]. Furthermore, dextran amines tolerate a wide variety of endogenous cellular glycosidases, and remains stable for up to 4 weeks after injection [147] because of their poly-(a-D-1,6-glucose) linkages [148]. Therefore, the use of dextran amine in this project can provide long-term and precise identification of regenerated axons.

In this project, the novel DA-CdTe:Gd QDs can be detected by both MRI and optical imaging techniques. Although the emission wavelength of my image probe can not provide deep tissue penetration ability, the emergence of near infrared (NIR) emitting QDs increases the optical penetration depth up to several centimeters [149]. My imaging probe provides a model for non-invasive neuronal tracer. In further studies, Gd-doped NIR emitting QDs can eventually achieve non-invasive neuronal tracing. Therefore, after the injection of magnetic QDs into injury area, we can observe regenerated neurons by both optical imaging and MRI. Although the use of QDs for neuronal tracing is still in the early stages, the future of this tool is bright.

CHAPTER 3

EXPERIMENTAL

3.1 Materials

Glutathione (GSH), $CdCl_2$•$2.5H_2O$, Na_2TeO_3, $NaBH_4$, $Gd(NO_3)_3$•$6H_2O$, 2-Propanol, Rhodamine 6G, HyClone™ DMEM/High glucose, fetal bovine serum (FBS), trypsin-EDTA and penicillin/streptomycin were purchased from Fisher Scientific (Ottawa, ON). N-hydroxysuccinimide (NHS), 1-ethyl-3-(3-dimethylaminopropyl) carbodiimide hydrochloride (EDC), and phosphate buffered saline (PBS) were purchased from Sigma-Aldrich (Oakville, ON). Dextran amine (DA, 10,000 MW), biotinylated dextran amines (BDA, 10,000 MW), and Vybrant® MTT cell proliferation assay kit, were purchased from Thermo Fisher Scientific (Burlington, ON). Mouse fibroblast cell line NIH/3T3 was purchased from American Type Culture Collection (ATCC, Manassas, USA). Quant*Tag™ Biotin quantitation kit (BDK-2000) was purchased from Vector

Laboratories Inc. (Burlington, ON). All other reagents were purchased from VWR International (Mississauga, ON) and used as received unless indicated otherwise.

3.2 Synthesis of CdTe:Gd QDs and Quantum Yield Measurements

Gadolinium doped CdTe QDs (CdTe:Gd QDs) were synthesized based on a previously published one-step refluxing route with minor modifications [150]. The molar ratios of reagents are slightly modified based on the previous study [150]. Specifically, 50 mL $CdCl_2{\bullet}2.5H_2O$ (9×10^{-4} mol) was first mixed with 20 mL GSH (1.2×10^{-3} mol) in a 250 mL four-necked flask at room temperature. Subsequently 2×10^{-4} mol Na_2TeO_3, 6×10^{-3} mol $NaBH_4$ and 6×10^{-5} mol $Gd(NO_3)_3{\bullet}6H_2O$ were added. The pH of the final reaction mixture was adjusted to 8.5 by dropwise adding NaOH. The pH value was measured by pH stripe. This resulting mixture was heated to 100 ℃. To monitor the progress of the reaction, small aliquots (approximately 15 mL) from the reaction were sampled at predetermined refluxing time intervals of 0, 5, 10, 20, 30, 50, 70, 90, 120, and 150 min. At the end of the reaction (refluxing time = 150 min), sampled QDs were washed and precipitated for 3 times by the addition of approximate 35 mL 2-Propanol to remove unreacted reagents. After adding 2-propanol, the polarity of solvent became weaker, so the QDs can gradually precipitate. Subsequently, samples were centrifuged at 3,724 g (Allegra® X-15R Centrifuge equipped with SX4750 router, Beckman Coulter, Pasadena CA) for 10 min. The resulting QD pellets were dried at 40 ℃ under vacuum for 24 h.

To test the effects of reaction pH on the properties of the precipitated QDs, reactions were also carried out at pH 9, 9.5 and 10 using the same methodology as described above. In a separate set of experiments, CdTe:Gd QDs with different Gd vs. Te feed ratios at 1:10, 3:10 and 5:10 were also synthesized (pH=9.5). All the experiments above are repeated for 2 times.

The optical properties (emission wavelength and QY) of prepared QDs were tested by UV-Vis absorbance spectrum and fluorescence spectrum

To determine the quantum yield (QY) of the resulting QDs, rhodamine 6G (R6G) was used as a reference with a known QY of 95% at an excitation wavelength of 490 nm [151]; the QY of CdTe:Gd QDs was evaluated using Eq.1:

$$\mathrm{QY_D} = \mathrm{QY_R}\left(\frac{\mathrm{A_R}}{\mathrm{A_D}}\right)\left(\frac{\mathrm{F_D}}{\mathrm{F_R}}\right)\left(\frac{\eta_\mathrm{D}}{\eta_\mathrm{R}}\right)^2 \qquad \text{Eq. [1]}$$

where QY is the quantum yield; A is the absorbance at the excitation wavelength of 490 nm; F is the area under the fluorescent spectra peak, and η is the refractive index of the solvent (R6G: ethanol; QD: water). Subscripts D and R indicate CdTe:Gd QD and R6G, respectively.

The peak intensity at the excitation wavelength of 490 nm can be read from absorption spectrum. The area under the fluorescent spectra peak can be calculated by Origin 8

(Origin Lab Corporation).

3.3 Surface Functionalization of CdTe:Gd QDs with DA and Characterization

DA molecules and CdTe QDs were conjugated via EDC and NHS as reported elsewhere with some modifications [52, 152]. In this project, all reagents were added simultaneously to prevent the self-polymerization of QDs. Amino groups of the DA molecules were used to react with the carboxyl groups on the QDs, as shown in Figure 8. Briefly, 2 mg/mL CdTe:Gd QDs were mixed with DA (MW 10,000) in PBS (pH = 7.4) at a DA to QDs molar ratio of 1:1 (DA: CdTe:Gd QDs = 1:1) on shaker. Subsequently, a solution of 0.2 M NHS and 0.08 M EDC was used to active the carboxylate groups on the CdTe:Gd QDs surface. To each milliliter of QDs solution, 100 μL of the EDC/NHS stock solution was added and the reaction mixture was allowed to react for 2 h at room temperature with gentle agitation. The resulting solution was purified by a 0.2 μm syringe filter and then further purified by Amicon® Ultra 0.5mL filters (100kD, Millipore Ltd., Etobicoke, ON) by ultracentrifugation at 14,000 g for 5 min to remove unreacted QDs and residual chemicals. The as-purified DA-CdTe: Gd QDs were stored at 4 ℃ for further experiments.

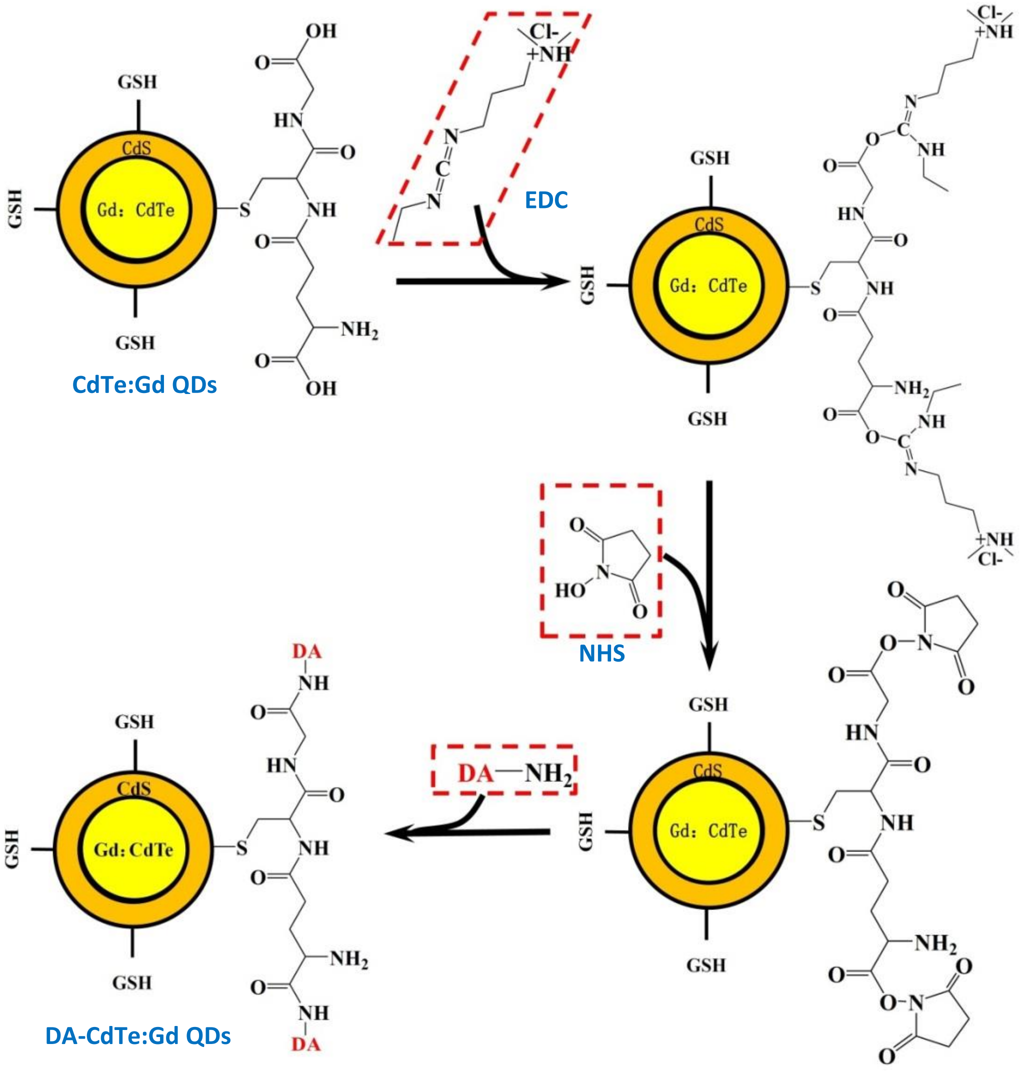

Figure 8. Schematic illustration for the synthesis of DA-CdTe:Gd QDs.

In order to investigate the effect of initial DA to CdTe:Gd QDs molar ratio on the final amount of conjugated DA molecules, biotinylated dextran amine (BDA, MW = 10,000) was used as a model molecule for DA so that it could be readily quantified using a commercial biotin kit. The biotin residue of BDA can react with kit reagents forming a colored product which can be quantified spectrophotometrically [153]. Therefore, the molar concentration of BDA on the coated QDs can be obtained by comparing the absorbance between test sample and standard biotin sample.

The molar concentrations of CdTe:Gd QDs and BDA-CdTe:Gd QDs were estimated according to Peng's empirical equation [154, 155] (Eq. [2]) and Lambert-Beer's law (Eq. [3]) as shown below:

$$D = (9.8127 \times 10^{-7})\lambda^3 - (1.7147 \times 10^{-3})\lambda^2 + (1.0064)\lambda - (194.84)$$

Eq. [2]

$$\varepsilon = 10043(D)^{2.12}$$

$$A = \varepsilon CL \qquad \text{Eq. [3]}$$

Where D (nm) is the size of QDs and λ (nm) and A are the wavelength and absorbance value of the absorption peak of corresponding QDs, respectively. ε (L/(mol•cm)) is the extinction coefficient per mole of QDs (both uncoated and coted QDs), and L (cm) is the path length of the beam of light used for recording UV-Vis absorbance spectrum. The value of L equals to 1 cm in our experiment. The molar concentration (C, mol/L) of samples can be derived eventually based on Lambert-Beer's law. This empirical equation has also been utilized elsewhere [156-158] to deduce the concentration of CdTe-based QDs. Lambert-Beer's law is considered valid under the experiment conditions.

3.4 Characterization

Optical properties were performed by UV-Vis absorbance spectrum with a Lambda 25 Perkin-Elmer spectrophotometer (Woodbridge, ON) and the fluorescence spectrum via a Horiba FluoroMax-4 Spectrofluorometer (Burlington, ON). X-ray powder diffraction (Rigaka Ultima IV Diffractometer) pattern was collected with Cu-Kα radiation from 10-80 ° 2θ. A high-resolution transmission electron microscope (HRTEM) was performed with JEM-2100F FE-TEM (JEOL) (Montreal, QC) to image the QDs' morphologies. The Acceleration voltage was 200 kV. Before HRTEM test, QDs were dispersed in ddH_2O and exposed to ultrasound for 10 min.

In order to test the magnetic behavior of prepared CdTe:Gd QDs and DA-CdTe:Gd QDs, T_1- and T_2- weighted MR images were recorded using a 7T Discovery MR901 pre-clinical MRI Scanner (GE/Agilent, Germany). For T_1 measurements, inversion recovery Look-Locker sequence with spoiled gradient echo was used (TE < 1 ms, TR= 2.4 ms). For T_2 measurements, spin-echo with multi-echo was used (TR = 6,000 ms).

During the XRD test, water protons were excited by a radiofrequency pulse. Subsequently, excited protons can return to their ground states in the magnetic field, which is referred as relaxation [159]. This process can be classified into two types: T_1 (longitudinal) relaxation and T_2 (transverse) relaxation [160]. The relaxivities (r_1 and r_2) are the measurement of the efficiency of an MRI contrast agent [161]. Relaxivity can be determined by Eq. [4]:

$$\frac{1}{T_{1,2,obs}} = \frac{1}{T_{1,2,dia}} + r_{1,2}[\mathrm{CA}] \qquad \text{Eq. [4]}$$

where $1/T_{1,\mathrm{dia}}$ and $1/T_{2,\mathrm{dia}}$ are the intrinsic longitudinal relaxation rate (R_1) and transverse relaxation rate (R_2) of water without the contrast agent, respectively. $1/T_{1,\text{obs}}$ and $1/T_{2,\text{obs}}$ represent the longitudinal relaxation rate (R_1) and transverse relaxation rate (R_2) of water in the presence of contrast agent. [CA] is the concentration of contrast agent. The relaxation rates are proportional to the concentration of contrast agent and the slope of a plot of $R_{1,2}$ versus [CA] is the relaxivity $r_{1,2}$.

3.5 Cytotoxicity Experiment

To study the cytotoxicity of the synthesized QDs, the mouse fibroblast cell line NIH/3T3 was used and the nanoparticles were sterilized by filtration which is recommended as a preferable sterilization technique for nanoparticles [162]. The cells were routinely cultured in HyClone™ DMEM/high glucose culture medium supplemented with 10% FBS and 1% penicillin/streptomycin at 37 ℃ with 5% CO2 air atmosphere. A MTT cell proliferation assay kit was use to evaluate the cytotoxicity of prepared DA-CdTe:Gd QDs with different initial DA to CdTe:Gd QDs molar ratios. Specifically, NIH/3T3 cells were seeded at a density of 1×104 cells per well in a 96-well culture plate and incubated for 24h. DA-CdTe:Gd QDs obtained at different initial DA to CdTe:Gd QDs ratios were dispersed in cell culture medium and added to each well to achieve the final concentrations of 0.0025, 0.01, 0.039, 0.156, 0.625 and 2.5 µM. As a control, the concentration of nanoparticle is 0 µM. Subsequently, cells were incubated in the presence of the nanoparticles for another 24 h. Finally, the cells were gently washed with fresh cell culture medium, and a MTT assay was performed to evaluate cell viability based on the vendor’s protocol. Each experiment was performed at least 5 times. Error bars indicate mean ± SD. ANOVA followed by t-test are applied to analyze statistical significance between groups and the control group (# $P < 0.05$). For pairwise comparison, t-test was used and the results are shown by the asterisk ($P \leqslant 0.05$) if the two groups are significantly different.

CHAPTER 4

RESULTS AND DISCUSSION

4.1 The Effect of pH on QD's Quantum Yield

The relationship between QYs of the QDs and emission wavelength at different pH are shown in Figure 9. The QY profiles show similar parabolic shapes for pH values of 8.5, 9.0 and 9.5, all peaking at a similar QY value of about 80%. In contrast, the profile for pH 10 does not exceed a QY of 50%. This result agrees well with a previous report that also studied CdTe QDs capped with GSH [163]. The effect of pH demonstrated in Figure 9 is likely due to the presence of GSH, a stabilizer used in the synthesis procedure, that forms a thiol-cadmium (GSH-Cd^{2+}) complex upon reacting with Cd^{2+}. This is mainly affected by pH [164]. For example, it is known that from alkalinity to pH 4 [165], GSH is more likely to complex with Cd on the surface of QDs, rather than with free Cd ions in reaction solution [164]. As a result, the formed Cd^{2+}-GSH complex on the QD surfaces occupies trap sites that have not been fully coordinated with Te atoms (Te atoms with dangling bond), which are mainly responsible for fluorescence quenching [163, 166]. Therefore, more defect sites are passivated by the Cd^{2+}-GSH complex and the QY is dramatically improved when pH is lower than 9.5. Furthermore, when the pH is less than or equal to 9.5, excess GSH could release S^{2-} gradually due to hydrolysis and combine with Cd^{2+} to form a CdS layer on the surface of QDs. The shell acts as a wide-bandgap material analogous to the CdS shell of CdSe/CdS core/shell QDs reported in [167, 168]. Therefore, the inorganic passivation effect of this CdS shell could eliminate dangling bonds of both Cd and Te atoms on the surface. Thus, the QY was improved with pH < 9.5. The formation of a CdS shell on the CdTe:Gd QDs is confirmed by the XRD test.

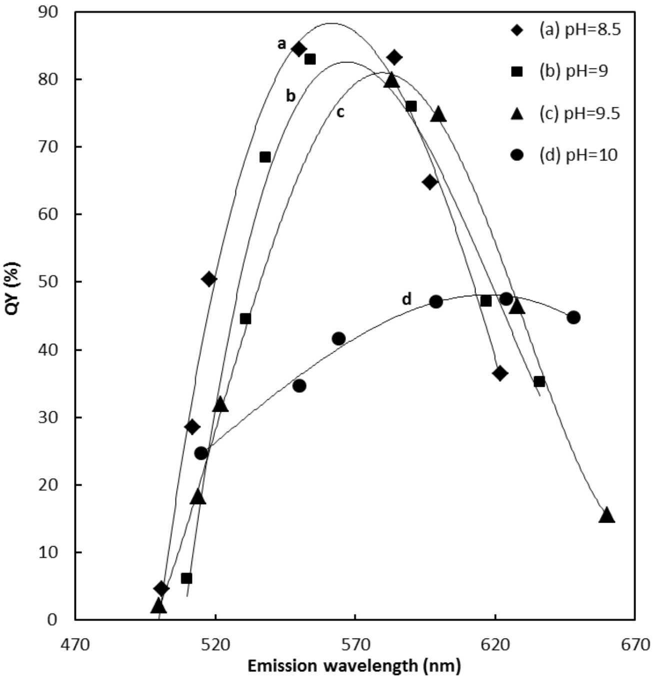

Figure 9. QY versus emission wavelength profiles for CdTe:Gd QDs synthesized at different pH values: (a) pH=8.5; (b) pH=9; (c) pH=9.5; (d) pH=10.

Although the sizes of QDs cannot be acquired directly from the experiment, QDs have size-dependent properties, for example larger QDs have narrower band gap and longer emission wavelength. Therefore, their size and growth rate can be estimated by their emission wavelength. As observed in Figure10, the higher the pH used in CdTe:Gd QDs synthesis was, the greater growth rate was based on the change of emission peak wavelength. It is because Gd:CdTe QDs are more tightly capped by the Cd^{2+}-GSH at lower pH values; the increased tight capping leads to a slower growth rate [163]. When pH value is 10, the QDs grow too quickly to have the quantum confinement effect when refluxing time of 150 min. Therefore, no fluorescence was observed for QDs prepared under refluxing time longer than 120 min at pH 10.

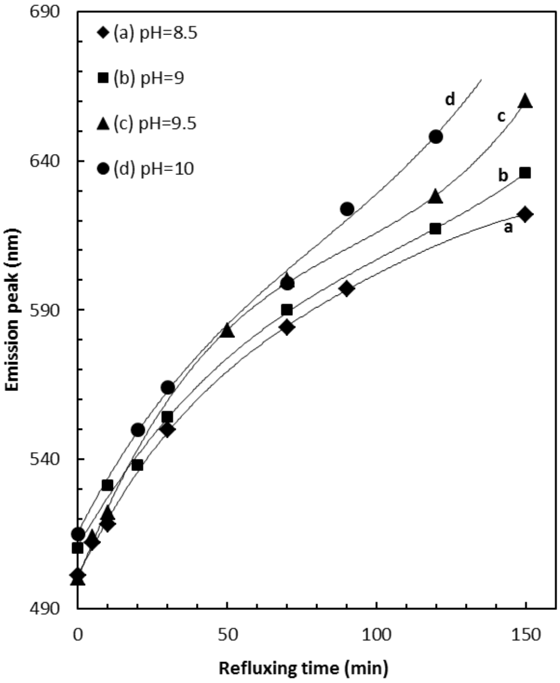

Figure 10. Growth rate of CdTe:Gd QDs in different synthesis pH values: (a) pH=8.5; (b) pH=9; (c) pH=9.5; (d) pH=1

In addition, as shown in Figure 11, the size of QDs that produced the maximum QY increased with increasing pH values. This result could be attributed to the Ostwald ripening mechanism. The reaction mixture, at any point during the reaction, is in constant growth and dissolution. The monomers prefer to occupy the positions at the surface and the large particles tend to dissolve from energetically favorable sites (e.g. defects, kinks) [166]. Therefore, when the growth and dissolution rate reach a equilibrium is where the maximum surface defects are eliminated and the highest quality QDs are produced [166]. Through affecting the tightness of the thiol-cap, the increasing pH seems to result in a shift of the dynamic equilibrium in our system.

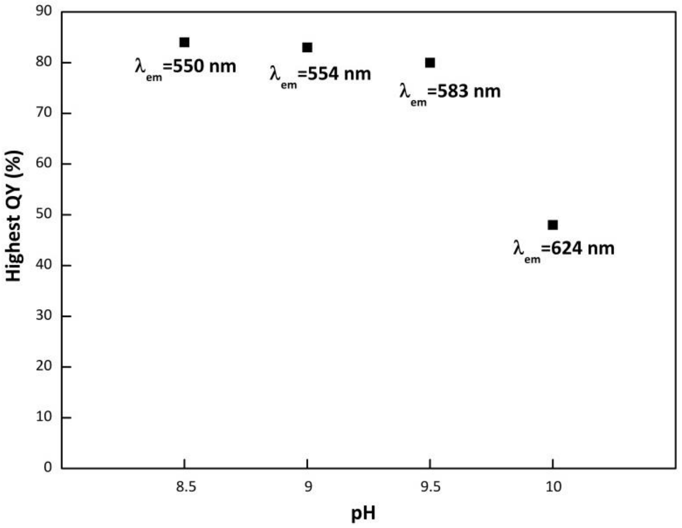

Figure 11. The highest QY under different pH values and their corresponding emission wavelength

Based on the results, it could be concluded that a decrease in QYs of QDs was observed as the reaction pH was increased from 9.5 to 10. However, when pH was within 8.5 to 9.5, the maximum QY value increased 4% only (from 84% to 80%). Thus, no obvious discernment can be made within that range. In clinical applications, auto-fluorescence (usually blue, green and yellow fluorescence) from tissue is the major obstacle of optical imaging. Therefore， pH=9.5 was chosen as the optimal pH condition, which generate relatively higher emission wavelength as the optimal pH. Under this pH value, the high emission wavelength will enhance fluorescence contrast, reduce the interference form auto-fluorescence and eventually effectively increase the sensitivity of optical imaging.

4.2 Determination of Optimal Gd/Te Molar Ratio

Gd/Te molar ratio is also an important factor that influenced the optical properties and MRI contrast effect of CdTe:Gd QDs [88, 169]. Low doping ratio could slightly enhance the florescence property of QDs, while large doping ratio could reduce the QYs of QDs [88]. As for the contrast effect, larger Gd doping ratio could theoretically increase the contrast effect [160]. The QY and the emission wavelength of QDs prepared under different Gd / Te ratios are shown in Figure 12. The Gd/Te ratios shown in Figure 12 are the feed ratios, however, the actual ratios in QDs can be assumed to be same based on previous study [88]. The QY profiles of QDs obtained at different Gd/ Te molar ratio have a parabolic shape when plotted as a function of emission wavelength (Figure 12 (A)).

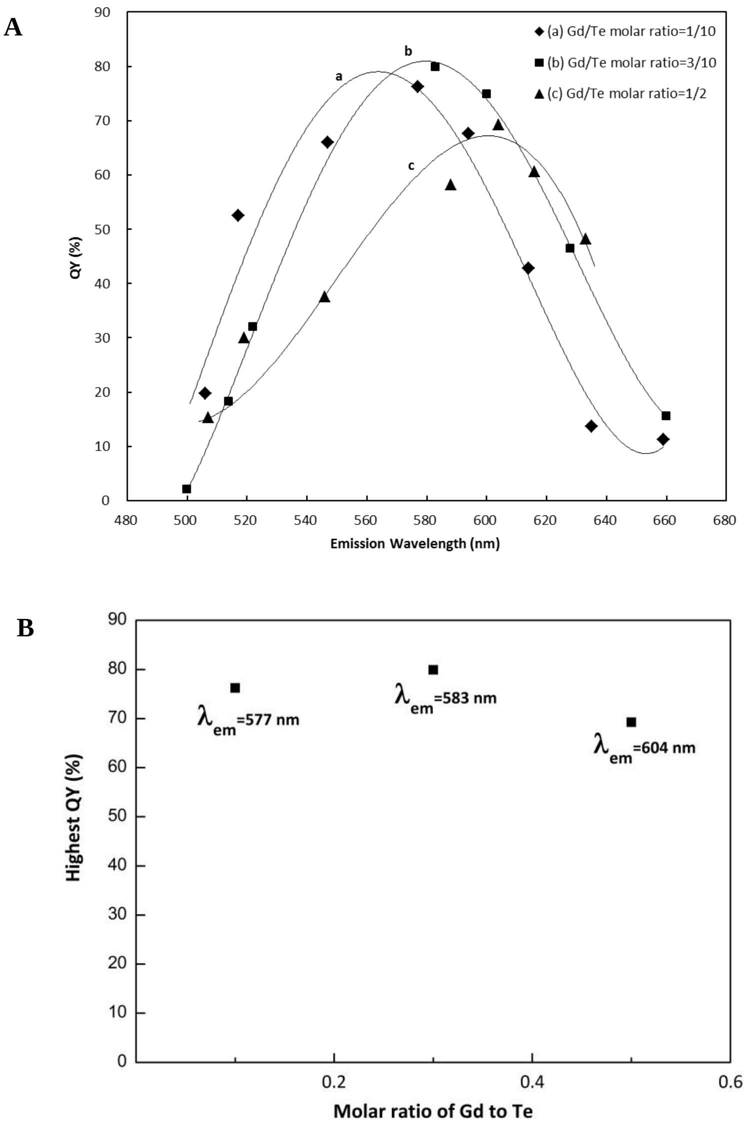

Figure 12. (A) QY of CdTe:Gd QDs with different Gd/Te molar ratios (B) The highest QY under different Gd/Te molar ratios and their corresponding emission wavelength.

Interestingly, as indicated in Figure 12 (B) when the Gd/Te ratio is 0.1, the maximum QY slightly increases from 76% to 80% with the increasing concentration of Gd to 0.3 ratio of Gd/Te. However, at Gd/Te ratios higher than 3/10, increasing Gd/Te ratio resulted in a decrease in the QY at a ratio of 0.5. When the Gd/Te ratio was to 1/2, the corresponding QY was 70%. Thus, when the Gd/Te ratio varied for 3 ratios, the QY maximum was for Gd/Te = 3/10. It has been demonstrated that oxidized Te atoms with dangling bonds on the surface are known to quench fluorescence and decrease QY [163, 166]. Therefore, at lower Gd concentrations, Gd atoms may reduce the number of Te atoms with dangling bonds by reduce the ratio of surface Te atoms. However, due to the different ionic radius of Gd^{3+} (0.938Å) and Cd^{2+} (0.97Å), the excessive Gd atom fraction in the QDs may result in an increasing surface roughness of QDs, which could generate more defects on the surface. [17, 123]. Therefore, when the Gd concentration is high, more defects could be created on the surface of QDs and correspondingly lead to the decrease of QY.

CdTe:Gd QDs exhibit not only fluorescence properties but also MRI contrast effects. The content of Gd is the critical factor that influences the MRI contrast effect. Gd:CdTe QDs in their role as MRI contrasting agents, relax the hydrogen atoms of water in the surrounding tissue. This relaxation enhances the contrast, and thus produces a better MR image [170].

The liner relationship between relaxation rate (R_1, R_2) and Gd concentration of CdTe:Gd QDs with different Gd/Te ratios, and relaxivities (r_1, r_2) of CdTe:Gd QDs with different Gd/Te ratios are demonstrated in Figure 13. Figures 13(A-F) indicate that the introduction of the Gd atom into the QD can accelerate both the longitudinal relaxation process (R_1) and the transverse relaxation process (R_2) of water protons. The longitudinal and transverse relaxivities (r_1 and r_2) of CdTe:Gd QDs are also increased with the increasing molar ratio of Gd to Te. Since Gd-based contrast agents are commonly T_1 contrast agents, thereby the effect on accelerating longitudinal relaxation process (r_1) will be studied. Gd-DTPA (Magnevist®) is a widely used gadolinium-based commercial MRI contrasting agent. At 7T, Magnevist® has an r_1 and r_2 values of 3.10 ± 0.01 and 5.4 $mM^{-1} \bullet s^{-1}$, respectively [171]. Figure 13 (G) shows that the longitudinal relaxivity (r_1) exceeds that of Magnevist when Gd to Te ratio is 1:2. r_1 values ranged from 2.9 $mM^{-1} \bullet s^{-1}$ with a Gd/Te ratio of 1:10 to 3.8 $mM^{-1} \bullet s^{-1}$ with a Gd/Te ratio of 1/2. The basic principle of Gd-based contrast agents is the coupling between electrons of Gd^{3+} and protons of surrounding water molecules. This interaction fades rapidly with distance [159]. Therefore, the higher Gd/Te ratio increase the interaction between Gd atoms and water molecules, resulting in a higher r_1.

Since r_1 value of CdTe:Gd QDs was higher than that of commercial contrast agents when Gd/Te = 1/2, the optimal Gd/Te ratio is chosen as 1/2 as the compromise for the QD to have both optical properties and MRI contrast effect. However it is notable that the highest QY of CdTe:Gd QDs obtained for Gd/Te=1/2 (69%) is higher than other magnetic doped QDs prepared by other groups, with QY≤ 40% [17, 123, 169]. Additionally, using CdTe:Gd QDs with the highest r_1 value (Gd/Te = 1/2) in pre-clinical trials would theoretically reduce the dosage of contrast agent [161], because there is a direct relationship between the dose of a contrast agent and its relaxation enhancement effect [161]. Thereby, the potential toxicity of CdTe:Gd QDs and cost of MRI scan can be reduced simultaneously [161].

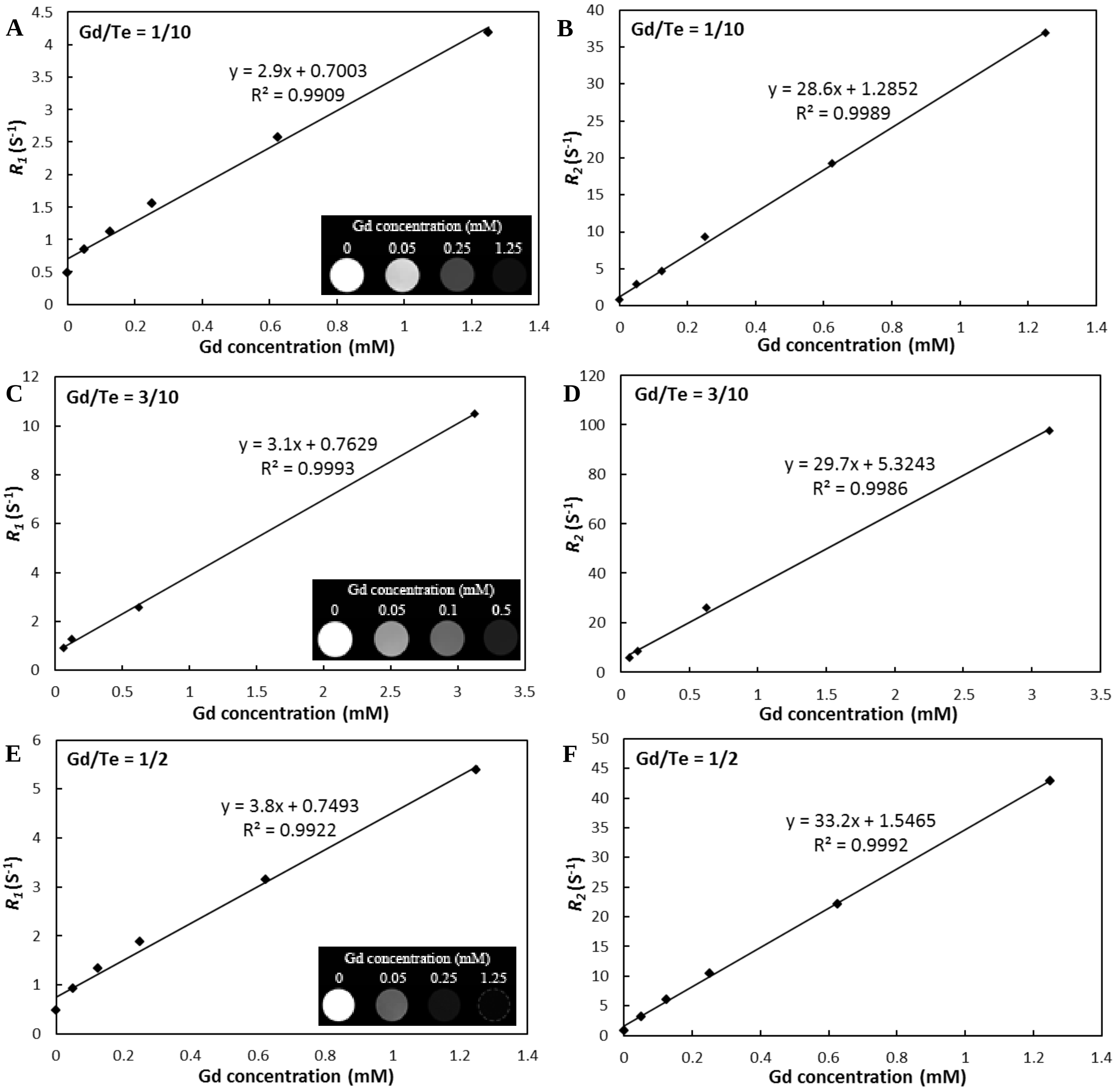

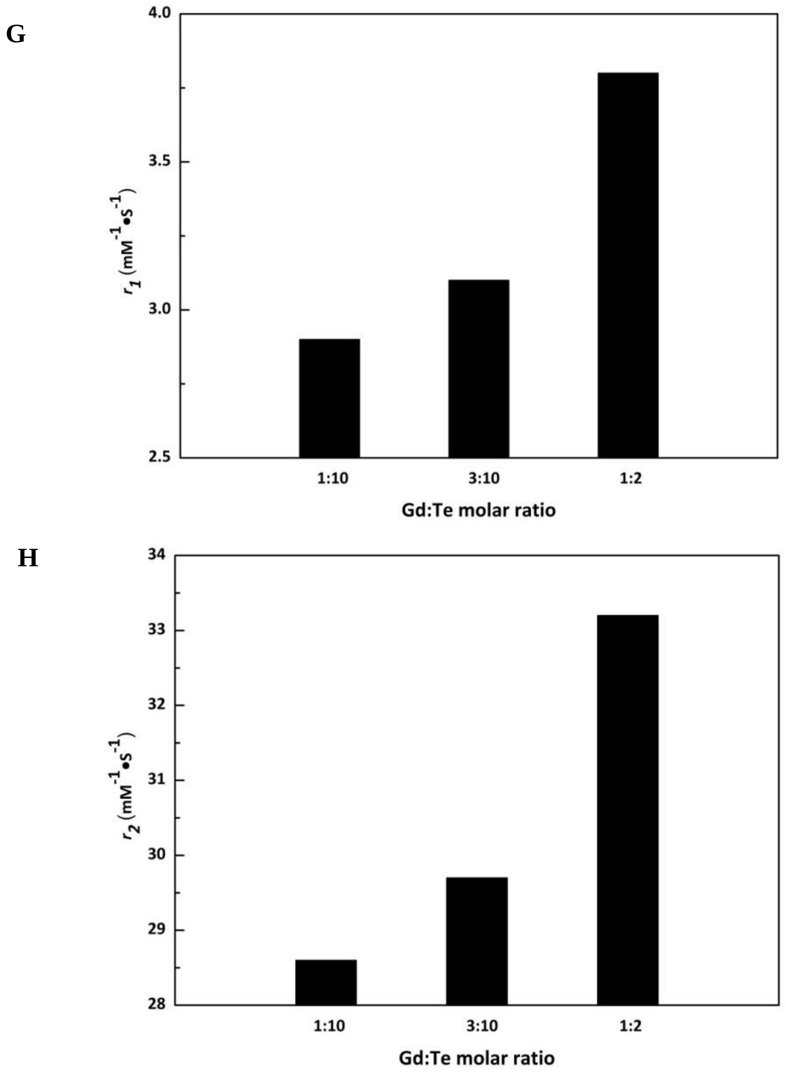

Figure 13. (A-F) R_1 (left) and R_2 (right) of CdTe:Gd QDs with different Gd/Te ratios at various Gd concentrations. The inset: T_2-weighted MR image of the corresponding Gd:CdTe QDs (distilled deionized water was used as control). Comparison of relaxivities of CdTe:Gd QDs with different Gd/Te ratios: r_1(G) and r_2 (H).

4.3 Characterizations of CdTe:Gd QDs Prepared Under Optimal Conditions

Aiming to have a better understanding of CdTe:Gd QDs obtained at optimal synthesis conditions (pH=9.5 Gd/Te=1/2), UV-Vis absorbance spectrum, fluorescence spectrum, HRTEM and XRD were used to investigate the optical properties, morphologies and crystalline structures of prepared uncoated QDs. The optical properties of prepared CdTe:Gd QDs are presented in Figure 14. As shown in Figure 14 (A), the absorption peaks are relatively narrow compared with other studies [172], which illustrate the fine particle size dispersion. Moreover, there is an evident red-shift of absorption wavelength from 457 nm to 600 nm with increasing refluxing time. Due to quantum confinement effect [173, 174], the bandgap of QDs become narrower as the size of QD increases. As a result, QDs can absorb and emit light with lower energy (longer wavelength). Therefore, the red-shift of absorption wavelength in Figure 14 (A) reveals that the sizes of CdTe:Gd QDs are growing with increasing refluxing time.

Similarly, the red-shift of emission wavelength shown in Figure 14 (B) further confirms that sizes of CdTe:Gd QDs could be tuned by adjusting refluxing time. The transparent solution of CdTe:Gd QDs in Figure 14 (C) indicated that prepared QDs are well-dispersed in double distilled deionized water without any post-treatment. Moreover, under UV excitation, these QDs emit intense fluorescence (Figure 14 (D)) which further confirms their excellent optical properties.

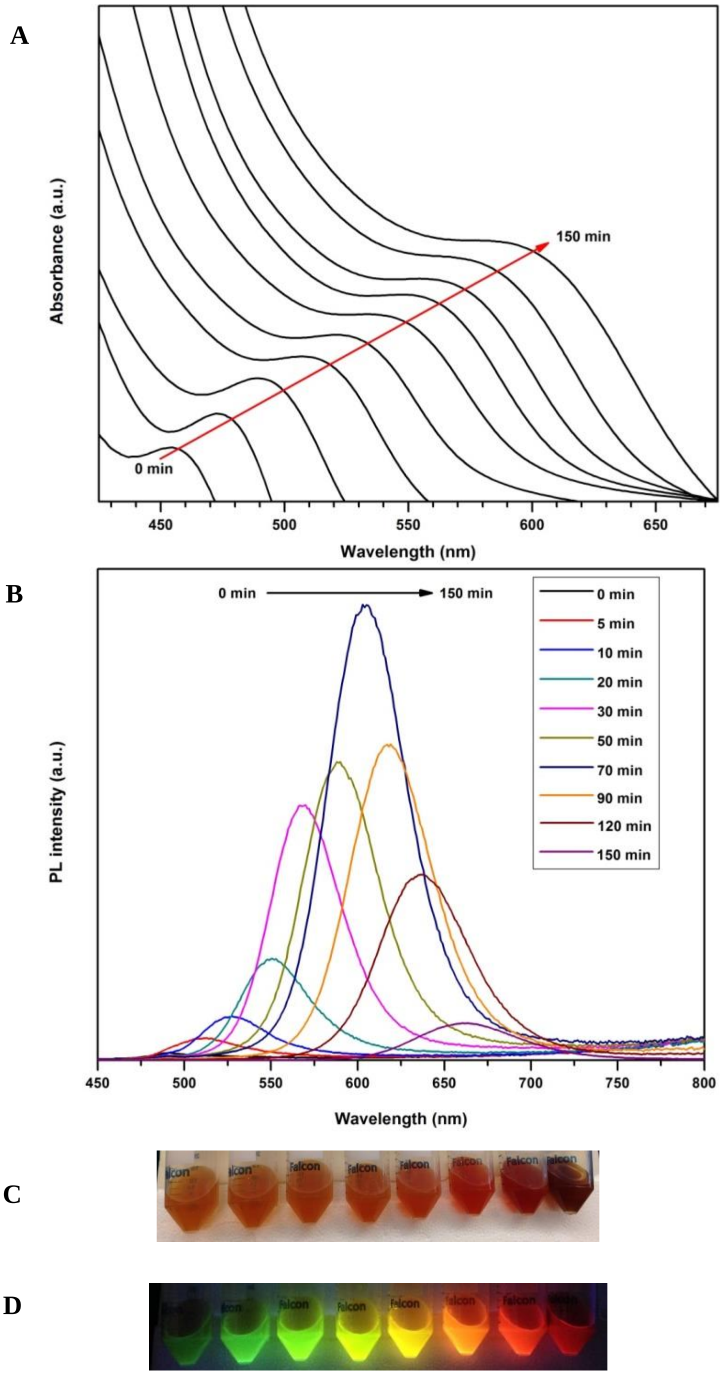

Figure 14. Absorption (A) and florescence, (B) spectra of CdTe:Gd QDs obtained at different refluxing time (λ_{ex}=420 nm); (C) images of prepared QDs under visible light and (D) 365nm UV irradiation.

Figure 15 provides a typical HRTEM image of CdTe:Gd QDs with an emission wavelength at 551 nm. It is evident that as-prepared QDs have a dot shape and good monodispersity compared with other studies [172]. The observed particle size is 2.5 ± 0.3 nm which is close to the size calculated from Peng's equation (3.25 nm) [155]. Furthermore, the existence of well resolved lattice planes also demonstrate good crystalline structure and high quality of synthesized CdTe:Gd QDs

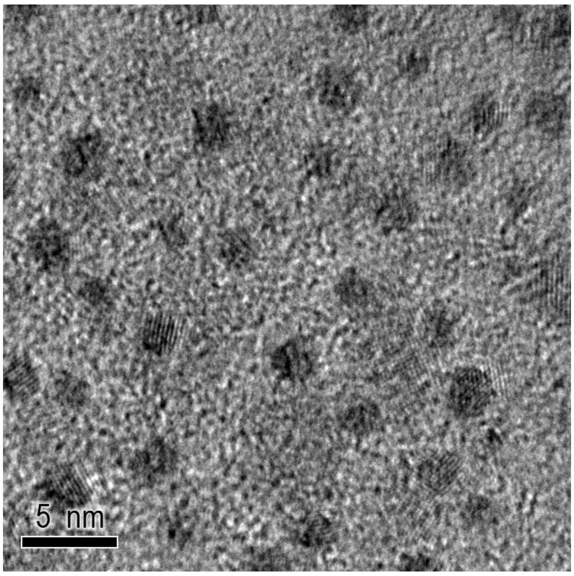

Figure 15. Representative HRTEM image of CdTe:Gd QDs (λ_{em}=551 nm).

As shown in Figure 16, the XRD pattern of prepared CdTe:Gd QDs is located between peak of bulk cubic CdTe and bulk cubic CdS. This is likely due to the formation of CdS shell on the surface of CdTe:Gd QDs. As mentioned in Section 4.1, partially coated GSH can slowly release S^{2-} ions from thiol group (-SH) over a prolonged refluxing time. Due to the electrostatic interaction, the released sulfur ion can combine with Cd^{2+} to form a CdS shell on prepared QDs [150, 163]. This shell can effectively eliminate the surface defects of the CdTe:Gd QDs and prevent the leaching of heavy metals (*e.g.* Cd, Te and Gd). As a result, reagent GSH not only serves as a stabilizer but also releases sulfur to be incorporated in the crystal of CdTe:Gd QDs. The XRD pattern agrees well with the XRD patterns obtained from other groups [88, 163, 175].

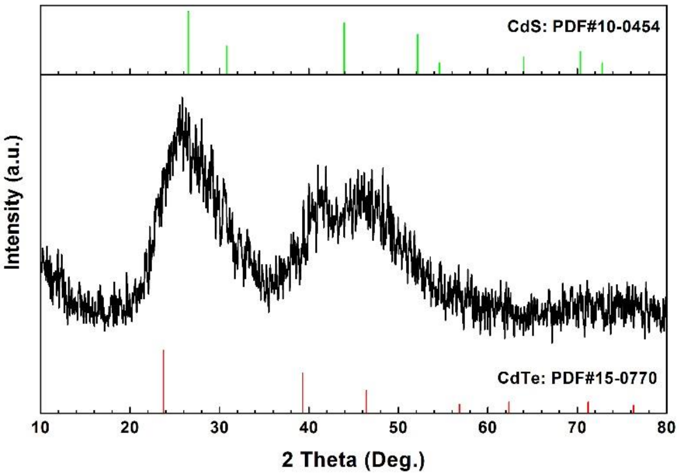

Figure 16. XRD pattern of CdTe:Gd QDs

4.4 The Effect of Initial DA to CdTe:Gd QDs Molar Ratio on the Final Amount of Conjugated DA Molecules

To acquire a non-invasive axonal tracing property, dextran amine (10,000 MW), a neuron tracer, was covalently linked to CdTe:Gd QDs. CdTe: Gd QDs used in this experiment were prepared under optimized synthesis conditions (pH=9.5, Gd/Te = 1/2). Based on previous studies, the number of coated molecules on the QDs surface plays an important role in the cytotoxicity of nanoparticles [176, 177]. Therefore, the number of conjugated DA molecules was investigated under different conjugation ratio of DA to CdTe:Gd QDs. The DA molecules and CdTe:Gd QDs were conjugated using EDC/NHS chemistry as reported previously with some modifications [52, 152, 178].

This method is competitive within variety bioconjugation methods because the resulting conjugates have the highest bioactivity [179-181].

In this part of the experiment, BDA was used as a model molecule for DA to investigate the effect of the initial DA to CdTe:Gd QDs molar ratio on the final amount of the conjugated DA molecules, as BDA can be easily quantified (Figure 17). As expected, the amount of conjugated BDA molecules per coated CdTe:Gd QDs ([BDA]/[BDA-CdTe:Gd QDs]) increased linearly as the initial BDA/CdTe:Gd QDs molar ratio increased from 1 to 20. However, further increase in the initial BDA/CdTe:Gd QDs molar ratio did not lead to a significant increase in the number of the conjugated BDA molecules on the nanoparticle surface. This saturation is most likely due to the limited number of carboxyl groups per CdTe:Gd QDs. It is interesting to note that commercially available carboxyl-functionalized QDs, Lake Placid Blue QDs (Evident Technologies) with similar size, are reported to have a similar number of carboxyl groups on the commercial QDs [182]. Furthermore, it is also likely that the steric hindrance of the bulky BDA molecules could also prevent further contact between unreacted BDA molecules and BDA-CdTe:Gd QDs. Thus, the number of the conjugated BDA molecules reached a plateau when the initial BDA/CdTe:Gd QDs molar ratio was 20.

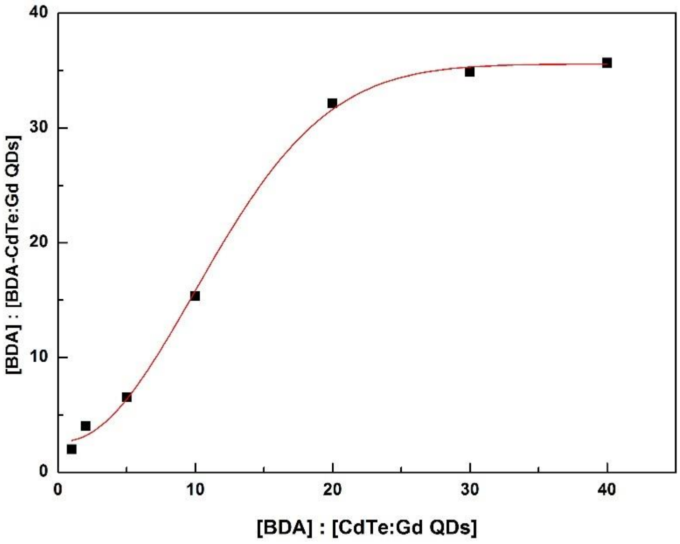

Figure 17. Correlation between the amount of conjugated BDA molecules and the initial BDA/CdTe:Gd QDs molar ratio.

4.5 Cytotoxicity of Prepared Multimodal Imaging Probe

The cytotoxicity is a critical factor to evaluate the feasibility of a new nanomaterial. In this project, the cytotoxicity of CdTe:Gd QDs and DA-CdTe:Gd QDs were assessed by using mouse fibroblast NIH/3T3 cells as a model with the MTT (methyl thiazolyl tetrazolium) assay. Since NIH/3T3 cells are commonly used for cytotoxicity experiment [183-186], so results comparison within these studies are easy and reliable. Compared with similar material [186], our nanoparticles have similar cell viability when the initial DA/CdTe:Gd QDs ratio is 20. Unless specified otherwise, conjugation ratio means initial DA/CdTe:Gd QDs ratio.

Nanoparticles were able to enter cells by receptor-mediated endocytosis which involves a variety of mechanisms such as caveolae-mediated endocytosis, clathrin-mediated endocytosis, clathrin- and caveolin-independent endocytosis [187]. The internalization mechanism of QDs might be mostly governed by clathrin-mediated endocytosis [188] and cellular uptake kinetics is size-dependent [189-191]. Based on previous studies [192, 193], the cellular uptake and exocytosis (removal process) of nanoparticles in the sub-100nm range reaches an equilibrium after 10 h. The cytotoxicity was therefore investigated after incubation of NIH/3T3 cells in the presence of QDs over 10 hours (usually 24h) as reported elsewhere [194] to acquire sufficient interactions between cells and as-prepared QDs (see Figure 18).

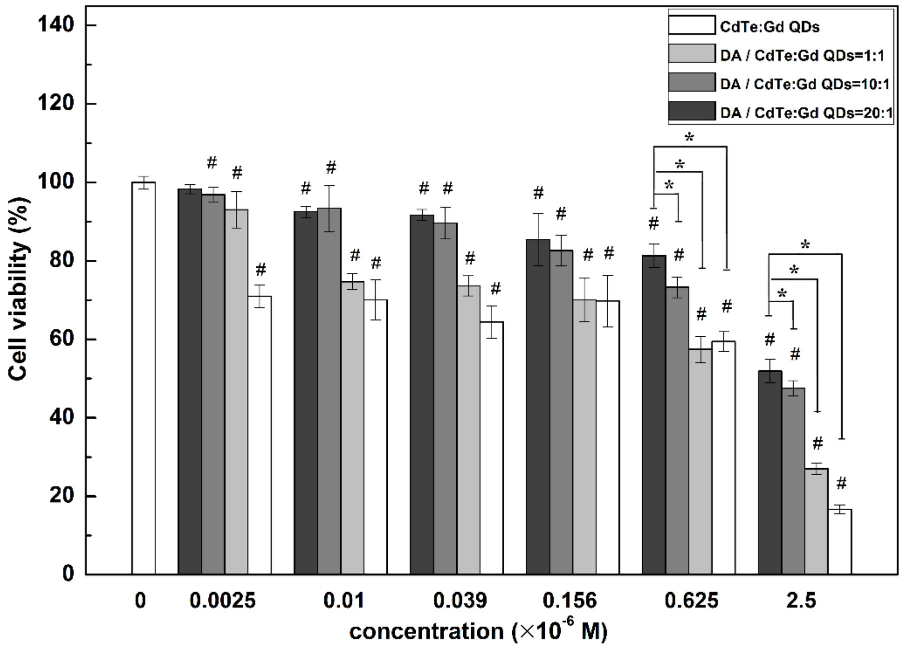

Figure 18. Cell viability of NIH/3T3 cells after incubated with CdTe:Gd QDs and DA-CdTe:Gd QDs obtained at different initial DA/CdTe:QDs ratios for 24 h by MTT assay. Groups significantly different from the control group (by ANOVA followed by t-test) are shown by # ($P<0.05$). Groups significantly different from the coated QDs (initial DA/CdTe:QDs=20) are shown by * ($P<0.05$).

It is evident that DA coated CdTe:Gd QDs demonstrate a better biocompatibility than uncoated CdTe:Gd QDs. Specifically, the cell viability of NIH/3T3 cells incubated with DA-CdTe:Gd QDs (conjugation ratio=20) was greater than 80% for QD concentrations up than 2.5 μM. Furthermore, pairwise comparisons between coated QDs prepared at conjugation ratio of 20 and other coated QDs indicate that at higher concentration (≥0.625 μM), coated QDs with the conjugation ratio of 20 have a statistically significant lower cytotoxicity compared with coated QDs with lower conjugation ratios (1 and 10). However, when the concentration of the coated QDs was reduced to 0.0025 μM, the cell viability of coated QDs with 3 different conjugation ratios all higher than 80%. This is likely because the concentration of the QDs is too low to show any cytotoxicity.

For uncoated CdTe:Gd QDs, they were more cytotoxic than coated QDs at all concentrations. The cell viability of uncoated CdTe:Gd QDs remained less than 72% regardless of the concentration used in this experiment. Based on these results, it can be concluded that DA coated QDs have better biocompatibility and when the amount of coated DA molecules is higher the cytotoxicity of DA-CdTe:Gd QDs is lower, especially when the initial DA/CdTe:Gd QDs ratio is 20. The oxidative stress induced by Cd^{2+} ions are considered as one of mechanisms of QDs cytotoxicity [195]. Reactive oxygen species (ROS) accompanied by oxidative stress trigger the cellular morphological changes of organelles and eventually cell death [195]. Therefore, the coverage of the nontoxic DA layer may prevent the leakage of Cd^{2+} from QDs improving biocompatibility. These results agree well with reported studies about functionalized QDs [176, 177]. As reported in reference [176] the cell viability of QDs increased 30% after surface functionalization of the QDs at a concentration of 20 nM.

4.6 Paramagnetism characterization and MR imaging of prepared multimodal imaging probe

On the basis of the surface density of DA molecules and cytotoxicity results, initial DA to CdTe:Gd QDs molar ratio was fixed at 20 and DA-CdTe:Gd QDs prepared with this condition were evaluated by a 7T MRI scanner to see the contrast property. The results are shown in Figure 19. The liner relationship between relaxation rate (R_1, R_2) and Gd concentration of DA-CdTe:Gd QDs suggests that r_1 relaxivity and r_2 relaxivity of functionalized CdTe:Gd QDs are higher than that of Magnevist®. The contrast effect of DA-CdTe:Gd QDs was confirmed in T_2-weighted images. Figure 19 (C) shows the negative contrast enhancement of functionalized CdTe:Gd QDs. However, as shown in Table 3, DA modifications on the QDs slightly reduced the contrast ability of nanoparticles. The reason of this is most likely because bulky DA molecules increase the spatial distance and steric hindrance between Gd atoms (electrons) in the QDs and the surrounding water molecules (protons), The interaction of electron-proton coupling fades with distance and the relaxivities are reduced as well [159].

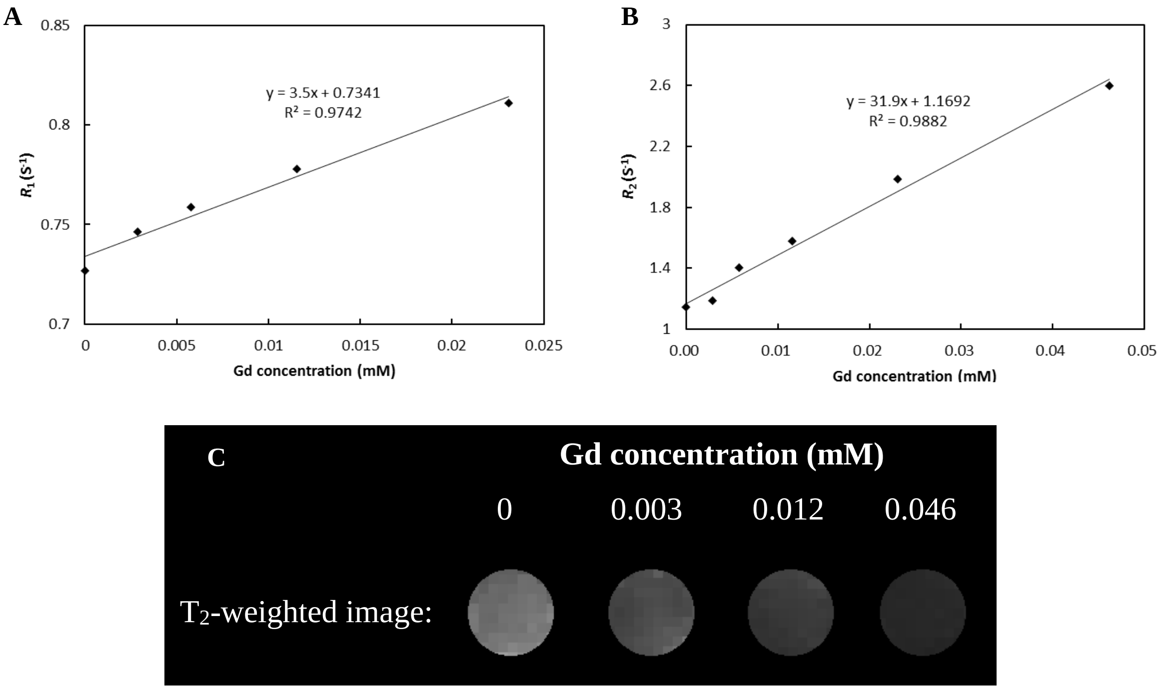

Figure 19. Contrast property of prepared DA-CdTe:Gd QDs measured in a 7 T MRI: (A) R1 (1/T1) determination of different DA-Gd:CdTe QDs concentrations suspended in PBS buffer. (B) R2 (1/T2) determination of different DA-Gd:CdTe QDs concentrations suspended in PBS buffer. (C) T2-weighted images of DA-Gd:CdTe QDs with different concentrations, PBS buffer was used as control.

Table 1

Contrast effect comparison between DA-CdTe:Gd QDs and commercial contrast agent (Magnevist®)

Contrast agent	Magnevist® (Gd-DTPA)	CdTe:Gd QDs	DA-CdTe:Gd QDs (DA/CdTe:Gd QDs=20)
$r_1 (mM^{-1}s^{-1})$	3.1	3.8	3.5
$r_2 (mM^{-1}s^{-1})$	5.4	33.2	31.9

CHAPTER 5

CONCLUSIONS AND FUTURE WORK

5.1 Project conclusions

In this project, water-soluble GSH capped Gd doped CdTe QDs (CdTe:Gd QDs) have been successfully synthesized by a one-step refluxing method. The synthesis conditions were optimized and determined by highest QY and MRI contrast effect. The resulting optimal conditions are: pH=9.5 and Gd/Te molar ratio = 1/2. The optical properties of as-prepared CdTe:Gd QDs were characterized by UV-Vis absorbance spectra and fluorescence spectra. Both spectra demonstrate the narrow QD size distribution and size-dependent optical properties. The size and structure of prepared CdTe:Gd QDs was confirmed by the TEM. The size of CdTe:Gd QDs was 2.5 ± 0.3 nm (λ_{em} = 551 nm). In addition, XRD results indicate the formation of a CdS shell on nanoparticle surface.

To use the QDs for non-invasive axonal tracing, DA molecules, a neuron tracer, was conjugated on the surface of CdTe:Gd QDs. During the conjugation process, the effect of the initial DA to CdTe:Gd QDs molar ratio on the final amount of conjugated DA molecules was investigated. The results show that the number of conjugated DA molecules per QDs is saturated when the initial DA to CdTe:Gd QDs molar ratio was 20. Furthermore, aiming to optimize the conjugation condition and evaluate the biocompatibility of DA-CdTe:Gd QDs, the cytotoxicity of CdTe:Gd QDs and DA coated CdTe:Gd QDs was tested with mouse fibroblast NIH/3T3 cells by MTT assay. The cytotoxicity experiment indicated that coated CdTe:Gd QDs have a better biocompatibility than uncoted CdTe:Gd QDs. In addition, coated QDs do not show evident cytotoxicity when the initial DA to CdTe:Gd QDs molar ratio is 20, which also suggests that the optimal conjugation ratio of DA to CdTe:Gd QDs is 20.

The MRI contrast effect of DA-CdTe:Gd QDs was tested to assess their potential ability as a non-invasive neuron tracer. Although the relaxivities of DA- CdTe:Gd QDs (r_1=3.5 $mM^{-1}s^{-1}$ and r_2=31.9 $mM^{-1}s^{-1}$) are slightly reduced compared with plain QDs, they are still higher than that of Magnevist® (r_1=3.1 $mM^{-1}s^{-1}$ and r_2=5.4 $mM^{-1}s^{-1}$) which is a commonly used commercial MRI contrast agent.

In conclusion, the as-prepared CdTe:Gd QDs possess excellent optical properties, crystal-structures and potential ability to be used as optical/MRI multimodal imaging probes. After surface functionalization with DA molecules, the DA- CdTe:Gd QDs retain a good contrast property and have good biocompatibility, which makes them well-suited for non-invasive axonal tracing. However, the available data are insufficient to conclude that our image probe is readily to be used in clinical studies. The heavy metal of QDs components still has potential risk to human bodies and the in vivo tracing effect need to be test in future studies. There is still a long way to go before applying QDs in human bodies, however, the future of this material is bright.

5.2 Future work

- Interference of auto-fluorescence from tissue and deep tissue penetration limit are the major obstacles blocking the potential applications of optical imaging. Therefore, further exploration of near-infrared optical imaging probes is more desirable.

- Heavy metals in the QD matrix increase the risk of applying as-prepared QDs in pre-clinical applications. Synthesizing QDs without heavy metal and with high quality is suggested for further studies.

- Although the preliminary cytotoxicity and MRI contrast effect of as-prepared multimodal imaging probes have been tested, their impact on normal tissue and in vivo tracing still need to be explored by animal experiments.

The employment of the novel multimodal imaging probes in pre-clinical trials requires more study. This project provides a conjugated high contrast potential application of multimodal imaging in non-invasive axonal tracing. Ultimately, it is hoped that this imaging probe will help us to better understand the axon regeneration mechanisms in real time without sacrificing animals at intervening time-points.

REFERENCES

[1] J.K. Willmann, N. van Bruggen, L.M. Dinkelborg, S.S. Gambhir, Molecular imaging in drug development, Nature Reviews Drug Discovery, 7 (2008) 591-607.

[2] J. Kim, Y. Piao, T. Hyeon, Multifunctional nanostructured materials for multimodal imaging, and simultaneous imaging and therapy, Chemical Society Reviews, 38 (2009) 372-390.

[3] L. Jing, K. Ding, S.V. Kershaw, I.M. Kempson, A.L. Rogach, M. Gao, Magnetically Engineered Semiconductor Quantum Dots as Multimodal Imaging Probes, Advanced Materials, 26 (2014) 6367-6386.

[4] J. Cheon, J.-H. Lee, Synergistically integrated nanoparticles as multimodal probes for nanobiotechnology, Accounts of chemical research, 41 (2008) 1630-1640.

[5] H. Kobayashi, M.R. Longmire, M. Ogawa, P.L. Choyke, Rational chemical design of the next generation of molecular imaging probes based on physics and biology: mixing modalities, colors and signals, Chemical Society Reviews, 40 (2011) 4626-4648.

[6] W.J.M. Mulder, G.J. Strijkers, G.A.F. van Tilborg, D.P. Cormode, Z.A. Fayad, K. Nicolay, Nanoparticulate Assemblies of Amphiphiles and Diagnostically Active Materials for Multimodality Imaging, Accounts of Chemical Research, 42 (2009) 904-914.

[7] P.D. Schellinger, H.M. Meinck, A. Thron, Diagnostic accuracy of MRI compared to CCT in patients with brain metastases, Journal of neuro-oncology, 44 (1999) 275-281.

[8] A. Bernaerts, F. Vanhoenacker, P. Parizel, J. Van Goethem, R. Van Altena, A. Laridon, J. De Roeck, V. Coeman, A. De Schepper, Tuberculosis of the central nervous system: overview of neuroradiological findings, European radiology, 13 (2003) 1876-

1890.

[9] R.J. Packer, R.A. Zimmerman, L.T. Bilaniuk, Magnetic resonance imaging in the evaluation of treatment‐related central nervous system damage, Cancer, 58 (1986) 635-640.

[10] M.E. Moseley, Y. Cohen, J. Kucharczyk, J. Mintorovitch, H.S. Asgari, M.F. Wendland, J. Tsuruda, D. Norman, Diffusion-weighted MR imaging of anisotropic water diffusion in cat central nervous system, Radiology, 176 (1990) 439-445.

[11] V. Dousset, C. Delalande, L. Ballarino, B. Quesson, D. Seilhan, M. Coussemacq, E. Thiaudiére, B. Brochet, P. Canioni, J.-M. Caillé, In vivo macrophage activity imaging in the central nervous system detected by magnetic resonance, Magnetic Resonance in Medicine, 41 (1999) 329-333.

[12] U. Bühring, U. Herrlinger, T. Krings, R. Thiex, M. Weller, W. Küker, MRI features of primary central nervous system lymphomas at presentation, Neurology, 57 (2001) 393-396.

[13] R. Kumar, M. Nyk, T.Y. Ohulchanskyy, C.A. Flask, P.N. Prasad, Combined Optical and MR Bioimaging Using Rare Earth Ion Doped NaYF4 Nanocrystals, Advanced Functional Materials, 19 (2009) 853-859.

[14] W. Feng, T. Wee Beng, Z. Yong, F. Xianping, W. Minquan, Luminescent nanomaterials for biological labelling, Nanotechnology, 17 (2006) R1.

[15] U. Resch-Genger, M. Grabolle, S. Cavaliere-Jaricot, R. Nitschke, T. Nann, Quantum dots versus organic dyes as fluorescent labels, Nature Methods, 5 (2008) 763-775.

[16] A.M. Derfus, A.A. Chen, D.-H. Min, E. Ruoslahti, S.N. Bhatia, Targeted Quantum Dot Conjugates for siRNA Delivery, Bioconjugate Chemistry, 18 (2007) 1391-1396.

[17] F. Zhang, T.-T. Sun, Y. Zhang, Q. Li, C. Chai, L. Lu, W. Shen, J. Yang, X.-W. He, Y.-K. Zhang, W.-Y. Li, Facile synthesis of functional gadolinium-doped CdTe quantum dots for tumor-targeted fluorescence and magnetic resonance dual-modality imaging, Journal of Materials Chemistry B, 2 (2014) 7201-7209.

[18] W.C.W. Chan, D.J. Maxwell, X. Gao, R.E. Bailey, M. Han, S. Nie, Luminescent quantum dots for multiplexed biological detection and imaging, Current Opinion in Biotechnology, 13 (2002) 40-46.

[19] B.N. Pal, I. Robel, A. Mohite, R. Laocharoensuk, D.J. Werder, V.I. Klimov, High-Sensitivity p–n Junction Photodiodes Based on PbS Nanocrystal Quantum Dots, Advanced Functional Materials, 22 (2012) 1741-1748.

[20] J.W. Stouwdam, R.A.J. Janssen, Red, green, and blue quantum dot LEDs with solution processable ZnO nanocrystal electron injection layers, Journal of Materials Chemistry, 18 (2008) 1889-1894.

[21] G.J. Stasiuk, S. Tamang, D. Imbert, C. Poillot, M. Giardiello, C. Tisseyre, E.L. Barbier, P.H. Fries, M. de Waard, P. Reiss, M. Mazzanti, Cell-Permeable Ln(III) Chelate-Functionalized InP Quantum Dots As Multimodal Imaging Agents, ACS Nano, 5 (2011) 8193-8201.

[22] T. Chifeng, Y. Yunhua, G. Mingyuan, Preparations of bifunctional polymeric beads simultaneously incorporated with fluorescent quantum dots and magnetic nanocrystals, Nanotechnology, 19 (2008) 105601.

[23] H. Gu, R. Zheng, X. Zhang, B. Xu, Facile One-Pot Synthesis of Bifunctional Heterodimers of Nanoparticles: A Conjugate of Quantum Dot and Magnetic Nanoparticles, Journal of the American Chemical Society, 126 (2004) 5664-5665.

[24] N. Pradhan, D.D. Sarma, Advances in Light-Emitting Doped Semiconductor

Nanocrystals, The Journal of Physical Chemistry Letters, 2 (2011) 2818-2826.

[25] H.S. Choi, W. Liu, F. Liu, K. Nasr, P. Misra, M.G. Bawendi, J.V. Frangioni, Design considerations for tumour-targeted nanoparticles, Nature Nanotechnology, 5 (2010) 42-47.

[26] G. Liang, D. Ye, X. Zhang, F. Dong, H. Chen, S. Zhang, J. Li, X. Shen, J. Kong, One-pot synthesis of Gd3+-functionalized gold nanoclusters for dual model (fluorescence/magnetic resonance) imaging, Journal of Materials Chemistry B, 1 (2013) 3545-3552.

[27] A.K. Saha, P. Sharma, H.-B. Sohn, S. Ghosh, R.K. Das, A.F. Hebard, H. Zeng, C. Baligand, G.A. Walter, B.M. Moudgil, Fe Doped CdTeS Magnetic Quantum Dots for Bioimaging(), Journal of materials chemistry. B, Materials for biology and medicine, 1 (2013) 6312-6320.

[28] I.F. Li, C.-S. Yeh, Synthesis of Gd doped CdSe nanoparticles for potential optical and MR imaging applications, Journal of Materials Chemistry, 20 (2010) 2079-2081.

[29] V. Chaudhry, J.D. Glass, J.W. Griffin, Wallerian degeneration in peripheral nerve disease, Neurol Clin, 10 (1992) 613-627.

[30] S. Jacobson, L. Guth, An electrophysiological study of the early stages of peripheral nerve regeneration, Experimental Neurology, 11 (1965) 48-60.

[31] G. Mukhopadhyay, P. Doherty, F.S. Walsh, P.R. Crocker, M.T. Filbin, A novel role for myelin-associated glycoprotein as an inhibitor of axonal regeneration, Neuron, 13 (1994) 757-767.

[32] M.S. Chen, A.B. Huber, M.E. van der Haar, M. Frank, L. Schnell, A.A. Spillmann, F. Christ, M.E. Schwab, Nogo-A is a myelin-associated neurite outgrowth inhibitor and an antigen for monoclonal antibody IN-1, Nature, 403 (2000) 434-439.

[33] D.A. Morgenstern, R.A. Asher, J.W. Fawcett, Chondroitin sulphate proteoglycans in the CNS injury response, Progress in Brain Research, 137 (2002) 313-332.

[34] R. McKeon, R. Schreiber, J. Rudge, J. Silver, Reduction of neurite outgrowth in a model of glial scarring following CNS injury is correlated with the expression of inhibitory molecules on reactive astrocytes, The Journal of Neuroscience, 11 (1991) 3398-3411.

[35] A. Subramanian, U.M. Krishnan, S. Sethuraman, Development of biomaterial scaffold for nerve tissue engineering: Biomaterial mediated neural regeneration, Journal of Biomedical Science, 16 (2009) 1-11.

[36] Y. Liu, D. Kim, B.T. Himes, S.Y. Chow, T. Schallert, M. Murray, A. Tessler, I. Fischer, Transplants of Fibroblasts Genetically Modified to Express BDNF Promote Regeneration of Adult Rat Rubrospinal Axons and Recovery of Forelimb Function, The Journal of Neuroscience, 19 (1999) 4370-4387.

[37] M. Oudega, T. Hagg, Nerve Growth Factor Promotes Regeneration of Sensory Axons into Adult Rat Spinal Cord, Experimental Neurology, 140 (1996) 218-229.

[38] J.C. Glover, G. Petursdottir, J.K.S. Jansen, Fluorescent dextran-amines used as axonal tracers in the nervous system of the chicken embryo, Journal of Neuroscience Methods, 18 (1986) 243-254.

[39] C.L. Veenman, A. Reiner, M.G. Honig, Biotinylated dextran amine as an anterograde tracer for single- and double-labeling studies, Journal of Neuroscience Methods, 41 (1992) 239-254.

[40] A. Puigdellívol-Sánchez, A. Valero-Cabré, A. Prats-Galino, X. Navarro, C. Molander, On the use of fast blue, fluoro-gold and diamidino yellow for retrograde tracing after peripheral nerve injury: uptake, fading, dye interactions, and toxicity,

Journal of Neuroscience Methods, 115 (2002) 115-127.

[41] E.C. Tsai, R.L. van Bendegem, S.W. Hwang, C.H. Tator, A Novel Method for Simultaneous Anterograde and Retrograde Labeling of Spinal Cord Motor Tracts in the Same Animal, Journal of Histochemistry & Cytochemistry, 49 (2001) 1111-1122.

[42] D.L. Sparks, L.-F. Lue, T.A. Martin, J. Rogers, Neural tract tracing using Di-I: a review and a new method to make fast Di-I faster in human brain, Journal of Neuroscience Methods, 103 (2000) 3-10.

[43] C.S. von Bartheld, D.E. Cunningham, E.W. Rubel, Neuronal tracing with DiI: decalcification, cryosectioning, and photoconversion for light and electron microscopic analysis, Journal of Histochemistry & Cytochemistry, 38 (1990) 725-733.

[44] A.J.M. Boulton, Whither Clinical Research in Diabetic Sensorimotor Peripheral Neuropathy?: Problems of end point selection for clinical trials, Diabetes Care, 30 (2007) 2752-2753.

[45] D.G. KLINE, Timing for Exploration of Nerve Lesions and Evaluation of the Neuroma-in-Continuity, Clinical Orthopaedics and Related Research, 163 (1982) 42-49.

[46] E. Gutmann, J.Z. Young, The re-innervation of muscle after various periods of atrophy, Journal of Anatomy, 78 (1944) 15-43.

[47] A. Reiner, M. Honig, Dextran Amines: Versatile Tools for Anterograde and Retrograde Studies of Nervous System Connectivity, in: L. Zaborszky, F. Wouterlood, J. Lanciego (Eds.) Neuroanatomical Tract-Tracing 3, Springer US, 2006, pp. 304-335.

[48] A.M. Smith, H. Duan, A.M. Mohs, S. Nie, Bioconjugated quantum dots for in vivo molecular and cellular imaging, Advanced drug delivery reviews, 60 (2008) 1226-1240.

[49] A.H. Mueller, M.A. Petruska, M. Achermann, D.J. Werder, E.A. Akhadov, D.D. Koleske, M.A. Hoffbauer, V.I. Klimov, Multicolor Light-Emitting Diodes Based on Semiconductor Nanocrystals Encapsulated in GaN Charge Injection Layers, Nano Letters, 5 (2005) 1039-1044.

[50] S. Santra, H. Yang, P.H. Holloway, J.T. Stanley, R.A. Mericle, Synthesis of Water-Dispersible Fluorescent, Radio-Opaque, and Paramagnetic CdS:Mn/ZnS Quantum Dots: A Multifunctional Probe for Bioimaging, Journal of the American Chemical Society, 127 (2005) 1656-1657.

[51] A. Hoshino, K.-i. Hanaki, K. Suzuki, K. Yamamoto, Applications of T-lymphoma labeled with fluorescent quantum dots to cell tracing markers in mouse body, Biochemical and Biophysical Research Communications, 314 (2004) 46-53.

[52] P. Wu, Y. He, H.-F. Wang, X.-P. Yan, Conjugation of Glucose Oxidase onto Mn-Doped ZnS Quantum Dots for Phosphorescent Sensing of Glucose in Biological Fluids, Analytical Chemistry, 82 (2010) 1427-1433.

[53] A. Ekimov, A. Onushchenko, Quantum size effect in three-dimensional microscopic semiconductor crystals, ZhETF Pisma Redaktsiiu, 34 (1981) 363.

[54] A.L. Efros, A.L. Efros, Interband absorption of light in a semiconductor sphere, Soviet Physics Semiconductors-Ussr, 16 (1982) 772-775.

[55] A. Ekimov, A. Onushchenko, Quantum size effect in the optical-spectra of semiconductor micro-crystals, Soviet Physics Semiconductors-Ussr, 16 (1982) 775-778.

[56] M. Reed, R. Bate, K. Bradshaw, W. Duncan, W. Frensley, J. Lee, H. Shih, Spatial quantization in GaAs–AlGaAs multiple quantum dots, Journal of Vacuum Science & Technology B, 4 (1986) 358-360.

[57] W.C. Chan, S. Nie, Quantum dot bioconjugates for ultrasensitive nonisotopic

detection, Science, 281 (1998) 2016-2018.

[58] M. Bruchez, M. Moronne, P. Gin, S. Weiss, A.P. Alivisatos, Semiconductor nanocrystals as fluorescent biological labels, Science, 281 (1998) 2013-2016.

[59] J.B. Delehanty, K. Susumu, R.L. Manthe, W.R. Algar, I.L. Medintz, Active cellular sensing with quantum dots: Transitioning from research tool to reality; a review, Analytica Chimica Acta, 750 (2012) 63-81.

[60] I. Yildiz, B. McCaughan, S.F. Cruickshank, J.F. Callan, F.M. Raymo, Biocompatible CdSe−ZnS Core−Shell Quantum Dots Coated with Hydrophilic Polythiols, Langmuir, 25 (2009) 7090-7096.

[61] E.S. Shibu, M. Hamada, S. Nakanishi, S.-i. Wakida, V. Biju, Photoluminescence of CdSe and CdSe/ZnS quantum dots: Modifications for making the invisible visible at ensemble and single-molecule levels, Coordination Chemistry Reviews, 263–264 (2014) 2-12.

[62] P. Juzenas, W. Chen, Y.-P. Sun, M.A.N. Coelho, R. Generalov, N. Generalova, I.L. Christensen, Quantum dots and nanoparticles for photodynamic and radiation therapies of cancer, Advanced Drug Delivery Reviews, 60 (2008) 1600-1614.

[63] P. Zrazhevskiy, M. Sena, X. Gao, Designing multifunctional quantum dots for bioimaging, detection, and drug delivery, Chemical Society Reviews, 39 (2010) 4326-4354.

[64] V.I. Klimov, Nanocrystal quantum dots-From fundamental photophysics to multicolor lasing, Los Alamos Science, 28 (2003) 214-220.

[65] E.J. McLaurin, M.S. Fataftah, D.R. Gamelin, One-step synthesis of alloyed dual-emitting semiconductor nanocrystals, Chemical Communications, 49 (2013) 39-41.

[66] B.O. Dabbousi, J. Rodriguez-Viejo, F.V. Mikulec, J.R. Heine, H. Mattoussi, R. Ober, K.F. Jensen, M.G. Bawendi, (CdSe)ZnS Core−Shell Quantum Dots: Synthesis and Characterization of a Size Series of Highly Luminescent Nanocrystallites, The Journal of Physical Chemistry B, 101 (1997) 9463-9475.

[67] T. Jamieson, R. Bakhshi, D. Petrova, R. Pocock, M. Imani, A.M. Seifalian, Biological applications of quantum dots, Biomaterials, 28 (2007) 4717-4732.

[68] M. Han, X. Gao, J.Z. Su, S. Nie, Quantum-dot-tagged microbeads for multiplexed optical coding of biomolecules, Nature Biotechnology, 19 (2001) 631-635.

[69] J.N. Mason, H. Farmer, I.D. Tomlinson, J.W. Schwartz, V. Savchenko, L.J. DeFelice, S.J. Rosenthal, R.D. Blakely, Novel fluorescence-based approaches for the study of biogenic amine transporter localization, activity, and regulation, Journal of Neuroscience Methods, 143 (2005) 3-25.

[70] J.E. Berlier, A. Rothe, G. Buller, J. Bradford, D.R. Gray, B.J. Filanoski, W.G. Telford, S. Yue, J. Liu, C.-Y. Cheung, W. Chang, J.D. Hirsch, J.M. Beechem Rosaria P. Haugland, R.P. Haugland, Quantitative Comparison of Long-wavelength Alexa Fluor Dyes to Cy Dyes: Fluorescence of the Dyes and Their Bioconjugates, Journal of Histochemistry & Cytochemistry, 51 (2003) 1699-1712.

[71] C. Eggeling, A. Volkmer, C.A.M. Seidel, Molecular Photobleaching Kinetics of Rhodamine 6G by One- and Two-Photon Induced Confocal Fluorescence Microscopy, ChemPhysChem, 6 (2005) 791-804.

[72] S.A. Soper, Q.L. Mattingly, Steady-State and Picosecond Laser Fluorescence Studies of Nonradiative Pathways in Tricarbocyanine Dyes: Implications to the Design of Near-IR Fluorochromes with High Fluorescence Efficiencies, Journal of the American Chemical Society, 116 (1994) 3744-3752.

[73] J. Riegler, P. Nick, U. Kielmann, T. Nann, Visualizing the Self-Assembly of Tubulin with Luminescent Nanorods, Journal of Nanoscience and Nanotechnology, 3 (2003) 380-385.

[74] A. Sukhanova, J. Devy, L. Venteo, H. Kaplan, M. Artemyev, V. Oleinikov, D. Klinov, M. Pluot, J.H.M. Cohen, I. Nabiev, Biocompatible fluorescent nanocrystals for immunolabeling of membrane proteins and cells, Analytical Biochemistry, 324 (2004) 60-67.

[75] Y. Zhang, J. He, P.-N. Wang, J.-Y. Chen, Z.-J. Lu, D.-R. Lu, J. Guo, C.-C. Wang, W.-L. Yang, Time-Dependent Photoluminescence Blue Shift of the Quantum Dots in Living Cells: Effect of Oxidation by Singlet Oxygen, Journal of the American Chemical Society, 128 (2006) 13396-13401.

[76] Z.A. Peng, X. Peng, Formation of High-Quality CdTe, CdSe, and CdS Nanocrystals Using CdO as Precursor, Journal of the American Chemical Society, 123 (2000) 183-184.

[77] D.V. Talapin, A.L. Rogach, A. Kornowski, M. Haase, H. Weller, Highly Luminescent Monodisperse CdSe and CdSe/ZnS Nanocrystals Synthesized in a Hexadecylamine−Trioctylphosphine Oxide−Trioctylphospine Mixture, Nano Letters, 1 (2001) 207-211.

[78] P. Reiss, J. Bleuse, A. Pron, Highly Luminescent CdSe/ZnSe Core/Shell Nanocrystals of Low Size Dispersion, Nano Letters, 2 (2002) 781-784.

[79] T. Rajh, O.I. Micic, A.J. Nozik, Synthesis and characterization of surface-modified colloidal cadmium telluride quantum dots, The Journal of Physical Chemistry, 97 (1993) 11999-12003.

[80] A.L. Rogach, L. Katsikas, A. Kornowski, D. Su, A. Eychmüller, H. Weller,

Synthesis and characterization of thiol-stabilized CdTe nanocrystals, Berichte der Bunsengesellschaft für physikalische Chemie, 100 (1996) 1772-1778.

[81] M. Gao, S. Kirstein, H. Möhwald, A.L. Rogach, A. Kornowski, A. Eychmüller, H. Weller, Strongly Photoluminescent CdTe Nanocrystals by Proper Surface Modification, The Journal of Physical Chemistry B, 102 (1998) 8360-8363.

[82] N. Gaponik, A.L. Rogach, Thiol-capped CdTe nanocrystals: progress and perspectives of the related research fields, Physical Chemistry Chemical Physics, 12 (2010) 8685-8693.

[83] D. Zhou, M. Lin, Z. Chen, H. Sun, H. Zhang, H. Sun, B. Yang, Simple Synthesis of Highly Luminescent Water-Soluble CdTe Quantum Dots with Controllable Surface Functionality, Chemistry of Materials, 23 (2011) 4857-4862.

[84] W.-C. Law, K.-T. Yong, I. Roy, H. Ding, R. Hu, W. Zhao, P.N. Prasad, Aqueous-Phase Synthesis of Highly Luminescent CdTe/ZnTe Core/Shell Quantum Dots Optimized for Targeted Bioimaging, Small, 5 (2009) 1302-1310.

[85] Y. Zheng, Z. Yang, Y. Li, J.Y. Ying, From Glutathione Capping to a Crosslinked, Phytochelatin-Like Coating of Quantum Dots, Advanced Materials, 20 (2008) 3410-3415.

[86] L. Zou, Z. Gu, N. Zhang, Y. Zhang, Z. Fang, W. Zhu, X. Zhong, Ultrafast synthesis of highly luminescent green- to near infrared-emitting CdTe nanocrystals in aqueous phase, Journal of Materials Chemistry, 18 (2008) 2807-2815.

[87] Z. Sheng, H. Han, X. Hu, C. Chi, One-step growth of high luminescence CdTe quantum dots with low cytotoxicity in ambient atmospheric conditions, Dalton Transactions, 39 (2010) 7017-7020.

[88] Q. Wang, T. Fang, P. Liu, B. Deng, X. Min, X. Li, Direct Synthesis of High-Quality

Water-Soluble CdTe:Zn2+ Quantum Dots, Inorganic Chemistry, 51 (2012) 9208-9213.

[89] H. Zhang, L. Wang, H. Xiong, L. Hu, B. Yang, W. Li, Hydrothermal Synthesis for High-Quality CdTe Nanocrystals, Advanced Materials, 15 (2003) 1712-1715.

[90] J. Guo, W. Yang, C. Wang, Systematic Study of the Photoluminescence Dependence of Thiol-Capped CdTe Nanocrystals on the Reaction Conditions, The Journal of Physical Chemistry B, 109 (2005) 17467-17473.

[91] L. Li, H. Qian, J. Ren, Rapid synthesis of highly luminescent CdTe nanocrystals in the aqueous phase by microwave irradiation with controllable temperature, Chemical Communications, (2005) 528-530.

[92] H. Qian, L. Li, J. Ren, One-step and rapid synthesis of high quality alloyed quantum dots (CdSe–CdS) in aqueous phase by microwave irradiation with controllable temperature, Materials Research Bulletin, 40 (2005) 1726-1736.

[93] H. Qian, X. Qiu, L. Li, J. Ren, Microwave-Assisted Aqueous Synthesis: A Rapid Approach to Prepare Highly Luminescent ZnSe(S) Alloyed Quantum Dots, The Journal of Physical Chemistry B, 110 (2006) 9034-9040.

[94] Y. He, H.-T. Lu, L.-M. Sai, W.-Y. Lai, Q.-L. Fan, L.-H. Wang, W. Huang, Microwave-Assisted Growth and Characterization of Water-Dispersed CdTe/CdS Core−Shell Nanocrystals with High Photoluminescence, The Journal of Physical Chemistry B, 110 (2006) 13370-13374.

[95] Y. He, H.-T. Lu, L.-M. Sai, Y.-Y. Su, M. Hu, C.-H. Fan, W. Huang, L.-H. Wang, Microwave Synthesis of Water-Dispersed CdTe/CdS/ZnS Core-Shell-Shell Quantum Dots with Excellent Photostability and Biocompatibility, Advanced Materials, 20 (2008) 3416-3421.

[96] W. Schumacher, A. Nagy, W.J. Waldman, P.K. Dutta, Direct Synthesis of Aqueous

CdSe/ZnS-Based Quantum Dots Using Microwave Irradiation, The Journal of Physical Chemistry C, 113 (2009) 12132-12139.

[97] H. Bao, N. Hao, Y. Yang, D. Zhao, Biosynthesis of biocompatible cadmium telluride quantum dots using yeast cells, Nano Research., 3 (2010) 481-489.

[98] D.-E. Lee, H. Koo, I.-C. Sun, J.H. Ryu, K. Kim, I.C. Kwon, Multifunctional nanoparticles for multimodal imaging and theragnosis, Chemical Society Reviews, 41 (2012) 2656-2672.

[99] A. Louie, Multimodality imaging probes: design and challenges, Chemical reviews, 110 (2010) 3146-3195.

[100] D.W. Townsend, J.P. Carney, J.T. Yap, N.C. Hall, PET/CT today and tomorrow, Journal of Nuclear Medicine, 45 (2004) 4S-14S.

[101] J. Zheng, G. Perkins, A. Kirilova, C. Allen, D.A. Jaffray, Multimodal contrast agent for combined computed tomography and magnetic resonance imaging applications, Investigative radiology, 41 (2006) 339-348.

[102] E. Pisani, N. Tsapis, B. Galaz, M. Santin, R. Berti, N. Taulier, E. Kurtisovski, O. Lucidarme, M. Ourevitch, B.T. Doan, Perfluorooctyl bromide polymeric capsules as dual contrast agents for ultrasonography and magnetic resonance imaging, Advanced Functional Materials, 18 (2008) 2963-2971.

[103] H. Xu, C.A. Regino, Y. Koyama, Y. Hama, A.J. Gunn, M. Bernardo, H. Kobayashi, P.L. Choyke, M.W. Brechbiel, Preparation and preliminary evaluation of a biotin-targeted, lectin-targeted dendrimer-based probe for dual-modality magnetic resonance and fluorescence imaging, Bioconjugate chemistry, 18 (2007) 1474-1482.

[104] V.S. Talanov, C.A. Regino, H. Kobayashi, M. Bernardo, P.L. Choyke, M.W. Brechbiel, Dendrimer-based nanoprobe for dual modality magnetic resonance and

fluorescence imaging, Nano letters, 6 (2006) 1459-1463.

[105] M. Nahrendorf, H. Zhang, S. Hembrador, P. Panizzi, D.E. Sosnovik, E. Aikawa, P. Libby, F.K. Swirski, R. Weissleder, Nanoparticle PET-CT imaging of macrophages in inflammatory atherosclerosis, Circulation, 117 (2008) 379-387.

[106] Y. Zhang, G.K. Das, R. Xu, T.T.Y. Tan, Tb-doped iron oxide: bifunctional fluorescent and magnetic nanocrystals, Journal of Materials Chemistry, 19 (2009) 3696-3703.

[107] D. Nagao, M. Yokoyama, N. Yamauchi, H. Matsumoto, Y. Kobayashi, M. Konno, Synthesis of highly monodisperse particles composed of a magnetic core and fluorescent shell, Langmuir, 24 (2008) 9804-9808.

[108] J. Yang, J. Lee, J. Kang, C.-H. Chung, K. Lee, J.-S. Suh, H.-G. Yoon, Y.-M. Huh, S. Haam, Magnetic sensitivity enhanced novel fluorescent magnetic silica nanoparticles for biomedical applications, Nanotechnology, 19 (2008) 075610.

[109] J.H. Lee, Y.w. Jun, S.I. Yeon, J.S. Shin, J. Cheon, Dual‐mode nanoparticle probes for high‐performance magnetic resonance and fluorescence imaging of neuroblastoma, Angewandte Chemie, 118 (2006) 8340-8342.

[110] Y.-S. Lin, S.-H. Wu, Y. Hung, Y.-H. Chou, C. Chang, M.-L. Lin, C.-P. Tsai, C.-Y. Mou, Multifunctional composite nanoparticles: magnetic, luminescent, and mesoporous, Chemistry of Materials, 18 (2006) 5170-5172.

[111] W. Cai, K. Chen, Z.-B. Li, S.S. Gambhir, X. Chen, Dual-function probe for PET and near-infrared fluorescence imaging of tumor vasculature, Journal of Nuclear Medicine, 48 (2007) 1862-1870.

[112] B. Fernandez, N. Galvez, R. Cuesta, A.B. Hungria, J.J. Calvino, J.M. Domínguez‐Vera, Quantum dots decorated with magnetic bionanoparticles,

Advanced Functional Materials, 18 (2008) 3931-3935.

[113] S. Wang, B.R. Jarrett, S.M. Kauzlarich, A.Y. Louie, Core/shell quantum dots with high relaxivity and photoluminescence for multimodality imaging, Journal of the American Chemical Society, 129 (2007) 3848-3856.

[114] M. Niedre, V. Ntziachristos, Elucidating structure and function in vivo with hybrid fluorescence and magnetic resonance imaging, Proceedings of the IEEE, 96 (2008) 382-396.

[115] T. Jin, Y. Yoshioka, F. Fujii, Y. Komai, J. Seki, A. Seiyama, Gd^{3+}-functionalized near-infrared quantum dots for in vivo dual modal (fluorescence/magnetic resonance) imaging, Chemical Communications, (2008) 5764-5766.

[116] L. Prinzen, R.-J.J. Miserus, A. Dirksen, T.M. Hackeng, N. Deckers, N.J. Bitsch, R.T. Megens, K. Douma, J.W. Heemskerk, M.E. Kooi, Optical and magnetic resonance imaging of cell death and platelet activation using annexin A5-functionalized quantum dots, Nano letters, 7 (2007) 93-100.

[117] M. Oostendorp, K. Douma, T.M. Hackeng, A. Dirksen, M.J. Post, M.A. van Zandvoort, W.H. Backes, Quantitative molecular magnetic resonance imaging of tumor angiogenesis using cNGR-labeled paramagnetic quantum dots, Cancer research, 68 (2008) 7676-7683.

[118] S.K. Mandal, N. Lequeux, B. Rotenberg, M. Tramier, J. Fattaccioli, J. Bibette, B. Dubertret, Encapsulation of magnetic and fluorescent nanoparticles in emulsion droplets, Langmuir, 21 (2005) 4175-4179.

[119] W.J.M. Mulder, R. Koole, R.J. Brandwijk, G. Storm, P.T.K. Chin, G.J. Strijkers, C. de Mello Donegá, K. Nicolay, A.W. Griffioen, Quantum Dots with a Paramagnetic Coating as a Bimodal Molecular Imaging Probe, Nano Letters, 6 (2006) 1-6.

[120] S. Pathak, E. Cao, M.C. Davidson, S. Jin, G.A. Silva, Quantum Dot Applications to Neuroscience: New Tools for Probing Neurons and Glia, The Journal of Neuroscience, 26 (2006) 1893-1895.

[121] H. Fan, E.W. Leve, C. Scullin, J. Gabaldon, D. Tallant, S. Bunge, T. Boyle, M.C. Wilson, C.J. Brinker, Surfactant-Assisted Synthesis of Water-Soluble and Biocompatible Semiconductor Quantum Dot Micelles, Nano Letters, 5 (2005) 645-648.

[122] Y.K. Lee, J.M. Jeong, L. Hoigebazar, B.Y. Yang, Y.-S. Lee, B.C. Lee, H. Youn, D.S. Lee, J.-K. Chung, M.C. Lee, Nanoparticles Modified by Encapsulation of Ligands with a Long Alkyl Chain to Affect Multispecific and Multimodal Imaging, Journal of Nuclear Medicine, 53 (2012) 1462-1470.

[123] Y. Liu, K. Ai, Q. Yuan, L. Lu, Fluorescence-enhanced gadolinium-doped zinc oxide quantum dots for magnetic resonance and fluorescence imaging, Biomaterials, 32 (2011) 1185-1192.

[124] H. Yang, Nanoparticle-Mediated Brain-Specific Drug Delivery, Imaging, and Diagnosis, Pharmaceutical Research, 27 (2010) 1759-1771.

[125] E.I. Sega, P.S. Low, Tumor detection using folate receptor-targeted imaging agents, Cancer and Metastasis Reviews, 27 (2008) 655-664.

[126] E.B. Voura, J.K. Jaiswal, H. Mattoussi, S.M. Simon, Tracking metastatic tumor cell extravasation with quantum dot nanocrystals and fluorescence emission-scanning microscopy, Nature Medicine, 10 (2004) 993-998.

[127] R.G. Thorne, C. Nicholson, In vivo diffusion analysis with quantum dots and dextrans predicts the width of brain extracellular space, Proceedings of the National Academy of Sciences, 103 (2006) 5567-5572.

[128] M. Dahan, S. Lévi, C. Luccardini, P. Rostaing, B. Riveau, A. Triller, Diffusion

Dynamics of Glycine Receptors Revealed by Single-Quantum Dot Tracking, Science, 302 (2003) 442-445.

[129] K. Kristensson, Y. Olsson, Retrograde axonal transport of protein, Brain Research, 29 (1971) 363-365.

[130] K. Kristensson, Y. Olsson, J. Sjöstrand, Axonal uptake and retrograde transport of exogenous proteins in the hypoglossal nerve, Brain Research, 32 (1971) 399-406.

[131] N.C. Veitch, Horseradish peroxidase: a modern view of a classic enzyme, Phytochemistry, 65 (2004) 249-259.

[132] S. Cullheim, J.-O. Kellerth, Combined light and electron microscopic tracing of neurons, including axons and synaptic terminals, after intracellular injection of horseradish peroxidase, Neuroscience Letters, 2 (1976) 307-313.

[133] K. Kristensson, Y. Olsson, Uptake and retrograde axonal transport of peroxidase in hypoglossal neurones, Acta Neuropathol, 19 (1971) 1-9.

[134] L. Novikova, L. Novikov, J.O. Kellerth, Persistent neuronal labeling by retrograde fluorescent tracers: a comparison between Fast Blue, Fluoro-Gold and various dextran conjugates, Journal of Neuroscience Methods, 74 (1997) 9-15.

[135] T. Naumann, W. Härtig, M. Frotscher, Retrograde tracing with Fluoro-Gold: different methods of tracer detection at the ultrastructural level and neurodegenerative changes of back-filled neurons in long-term studies, Journal of Neuroscience Methods, 103 (2000) 11-21.

[136] S. Schnell, M. Wessendorf, Bisbenzimide: a fluorescent counterstain for tissue autoradiography, Histochemistry and Cell Biology, 103 (1995) 111-114.

[137] I. Nicoletti, G. Migliorati, M.C. Pagliacci, F. Grignani, C. Riccardi, A rapid and

simple method for measuring thymocyte apoptosis by propidium iodide staining and flow cytometry, Journal of Immunological Methods, 139 (1991) 271-279.

[138] M. Bentivoglio, H.G.J.M. Kuypers, C.E. Catsman-Berrevoets, H. Loewe, O. Dann, Two new fluorescent retrograde neuronal tracers which are transported over long distances, Neuroscience Letters, 18 (1980) 25-30.

[139] H.G.J.M. Kuypers, C.E. Catsman-Berrevoets, R.E. Padt, Retrograde anoxal transport of fluorescent substances in the rat's forebrain, Neuroscience Letters, 6 (1977) 127-133.

[140] M. Bentivoglio, H.G.J.M. Kuypers, C.E. Catsman-Berrevoets, Retrograde neuronal labeling by means of bisbenzimide and Nuclear Yellow (Hoechst S 769121). Measures to prevent diffusion of the tracers out of retrogradely labeled neurons, Neuroscience Letters, 18 (1980) 19-24.

[141] F. Condé, Further studies on the use of the fluorescent tracers fast blue and diamidino yellow: Effective uptake area and cellular storage sites, Journal of Neuroscience Methods, 21 (1987) 31-43.

[142] B.R. Arenkiel, Neural Tracing Methods : Tracing Neurons and Their Connections, Springer New York, New York, NY, 2015.

[143] H.M. Brandt, A.V. Apkarian, Biotin-dextran: a sensitive anterograde tracer for neuroanatomic studies in rat and monkey, Journal of Neuroscience Methods, 45 (1992) 35-40.

[144] A. Reiner, C.L. Veenman, L. Medina, Y. Jiao, N. Del Mar, M.G. Honig, Pathway tracing using biotinylated dextran amines, Journal of Neuroscience Methods, 103 (2000) 23-37.

[145] P. Weiss, H.B. Hiscoe, Experiments on the mechanism of nerve growth, Journal

of Experimental Zoology, 107 (1948) 315-395.

[146] X. Jiang, R.R. Johnson, A. Burkhalter, Visualization of dendritic morphology of cortical projection neurons by retrograde axonal tracing, Journal of Neuroscience Methods, 50 (1993) 45-60.

[147] J.L. Lanciego, F.G. Wouterlood, A half century of experimental neuroanatomical tracing, Journal of Chemical Neuroanatomy, 42 (2011) 157-183.

[148] H. Lyon, P. Prentoe, Haugland RP. Handbook of flourescent probes and research chemicals, Ugeskrift for laeger 159 (1997) 4285-4285.

[149] E. Cassette, M. Helle, L. Bezdetnaya, F. Marchal, B. Dubertret, T. Pons, Design of new quantum dot materials for deep tissue infrared imaging, Advanced Drug Delivery Reviews, 65 (2013) 719-731.

[150] Z. Sheng, H. Han, X. Hu, C. Chi, One-step growth of high luminescence CdTe quantum dots with low cytotoxicity in ambient atmospheric conditions, Dalton Trans., 39 (2010) 7017-7020.

[151] M. Grabolle, M. Spieles, V. Lesnyak, N. Gaponik, A. Eychmüller, U. Resch-Genger, Determination of the Fluorescence Quantum Yield of Quantum Dots: Suitable Procedures and Achievable Uncertainties, Analytical Chemistry, 81 (2009) 6285-6294.

[152] A.C. Vinayaka, M.S. Thakur, Photoabsorption and resonance energy transfer phenomenon in CdTe− protein bioconjugates: An insight into QD− biomolecular interactions, Bioconjugate chemistry, 22 (2011) 968-975.

[153] B. Kanagy, An Accurate and Simple Spectrophotometric Assay System for Quantitation of Biotin: The Quant* Tag™ Biotin Kit, (2013).

[154] W.W. Yu, L. Qu, W. Guo, X. Peng, Experimental Determination of the Extinction

Coefficient of CdTe, CdSe and CdS Nanocrystals, Chemistry of Materials, 16 (2004) 560-560.

[155] W.W. Yu, L. Qu, W. Guo, X. Peng, Experimental determination of the extinction coefficient of CdTe, CdSe, and CdS nanocrystals, Chemistry of Materials, 15 (2003) 2854-2860.

[156] J. Xiao, L. Chen, F. Yang, C. Liu, Y. Bai, Green, yellow and red emitting CdTe QDs decreased the affinities of apigenin and luteolin for human serum albumin in vitro, Journal of hazardous materials, 182 (2010) 696-703.

[157] S.C. Pu, M.J. Yang, C.C. Hsu, C.W. Lai, C.C. Hsieh, S.H. Lin, Y.M. Cheng, P.T. Chou, The Empirical Correlation Between Size and Two‐Photon Absorption Cross Section of CdSe and CdTe Quantum Dots, Small, 2 (2006) 1308-1313.

[158] J. Xiao, T. Chen, L. Chen, H. Cao, F. Yang, Y. Bai, CdTe quantum dots (QDs) improve the affinities of baicalein and genistein for human serum albumin in vitro, Journal of inorganic biochemistry, 104 (2010) 1148-1155.

[159] R. Koole, W.J.M. Mulder, M.M. van Schooneveld, G.J. Strijkers, A. Meijerink, K. Nicolay, Magnetic quantum dots for multimodal imaging, Wiley Interdisciplinary Reviews: Nanomedicine and Nanobiotechnology, 1 (2009) 475-491.

[160] D. Weishaupt, V.D. Köchli, B. Marincek, How does MRI work?: an introduction to the physics and function of magnetic resonance imaging, Springer Science & Business Media, 2008.

[161] D. Weishaupt, J.M. Froehlich, D. Nanz, V.D. Köchli, K.P. Pruessmann, B. Marincek, How does MRI work?: An Introduction to the Physics and Function of Magnetic Resonance Imaging, Springer Berlin Heidelberg, 2013.

[162] M.A. Vetten, C.S. Yah, T. Singh, M. Gulumian, Challenges facing sterilization

and depyrogenation of nanoparticles: Effects on structural stability and biomedical applications, Nanomedicine: Nanotechnology, Biology and Medicine, 10 (2014) 1391-1399.

[163] H. Qian, C. Dong, J. Weng, J. Ren, Facile One-Pot Synthesis of Luminescent, Water-Soluble, and Biocompatible Glutathione-Coated CdTe Nanocrystals, Small, 2 (2006) 747-751.

[164] V. Swayambunathan, D. Hayes, K.H. Schmidt, Y.X. Liao, D. Meisel, Thiol surface complexation on growing cadmium sulfide clusters, Journal of the American Chemical Society, 112 (1990) 3831-3837.

[165] H.-B. Bürgi, Stereochemistry of Polynuclear Cadmium(II) Thioglycolates: Crystal structure of cadmium(II) bisthioglycolate, Helvetica Chimica Acta, 57 (1974) 513-519.

[166] H. Borchert, D.V. Talapin, N. Gaponik, C. McGinley, S. Adam, A. Lobo, T. Möller, H. Weller, Relations between the Photoluminescence Efficiency of CdTe Nanocrystals and Their Surface Properties Revealed by Synchrotron XPS, The Journal of Physical Chemistry B, 107 (2003) 9662-9668.

[167] X. Peng, M.C. Schlamp, A.V. Kadavanich, A.P. Alivisatos, Epitaxial Growth of Highly Luminescent CdSe/CdS Core/Shell Nanocrystals with Photostability and Electronic Accessibility, Journal of the American Chemical Society, 119 (1997) 7019-7029.

[168] J.J. Li, Y.A. Wang, W. Guo, J.C. Keay, T.D. Mishima, M.B. Johnson, X. Peng, Large-Scale Synthesis of Nearly Monodisperse CdSe/CdS Core/Shell Nanocrystals Using Air-Stable Reagents via Successive Ion Layer Adsorption and Reaction, Journal of the American Chemical Society, 125 (2003) 12567-12575.

[169] W. Guo, W. Yang, Y. Wang, X. Sun, Z. Liu, B. Zhang, J. Chang, X. Chen, Color-tunable Gd-Zn-Cu-In-S/ZnS quantum dots for dual modality magnetic resonance and fluorescence imaging, Nano Research., 7 (2014) 1581-1591.

[170] S. Dumas, V. Jacques, W.-C. Sun, J.S. Troughton, J.T. Welch, J.M. Chasse, H. Schmitt-Willich, P. Caravan, High relaxivity MRI contrast agents part 1: Impact of single donor atom substitution on relaxivity of serum albumin-bound gadolinium complexes, Investigative radiology, 45 (2010) 600-612.

[171] C. Kalavagunta, G. Metzger, A field comparison of r1 and r2* relaxivities of Gd-DTPA in aqueous solution and whole blood: 3 T versus 7 T, Proc ISMRM, 18 (2010).

[172] L.-N. Chen, J. Wang, W.-T. Li, H.-Y. Han, Aqueous one-pot synthesis of bright and ultrasmall CdTe/CdS near-infrared-emitting quantum dots and their application for tumor targeting in vivo, Chemical Communications, 48 (2012) 4971-4973.

[173] K.M. Gattás-Asfura, R.M. Leblanc, Peptide-coated CdS quantum dots for the optical detection of copper (II) and silver (I), Chemical Communications, (2003) 2684-2685.

[174] Q. Wang, T. Fang, P. Liu, B. Deng, X. Min, X. Li, Direct Synthesis of High-Quality Water-Soluble CdTe: Zn2+ Quantum Dots, Inorganic chemistry, 51 (2012) 9208-9213.

[175] Y. He, L.-M. Sai, H.-T. Lu, M. Hu, W.-Y. Lai, Q.-L. Fan, L.-H. Wang, W. Huang, Microwave-Assisted Synthesis of Water-Dispersed CdTe Nanocrystals with High Luminescent Efficiency and Narrow Size Distribution, Chemistry of Materials, 19 (2007) 359-365.

[176] X. Jiang, M. Ahmed, Z. Deng, R. Narain, Biotinylated Glyco-Functionalized Quantum Dots: Synthesis, Characterization, and Cytotoxicity Studies, Bioconjugate

Chemistry, 20 (2009) 994-1001.

[177] L. Zhou, C. Gao, W. Xu, X. Wang, Y. Xu, Enhanced Biocompatibility and Biostability of CdTe Quantum Dots by Facile Surface-Initiated Dendritic Polymerization, Biomacromolecules, 10 (2009) 1865-1874.

[178] S. Wang, N. Mamedova, N.A. Kotov, W. Chen, J. Studer, Antigen/antibody immunocomplex from CdTe nanoparticle bioconjugates, Nano letters, 2 (2002) 817-822.

[179] M.I. HALLIDAY, G.B. WISDOM, A comparison of three methods for the preparation of enzyme-antibody conjugates, Biochemical Society Transactions, 14 (1986) 473-474.

[180] M. Imagawa, S. Yoshitake, Y. Hamaguchi, E. Ishikawa, Y. Niitsu, I. Urushizaki, R. Kanazawa, S. Tachibana, N. Nakazawa, H. Ogawa, Characteristics and evaluation of antibody-horseradish peroxidase conjugates prepared by using a maleimide compound, glutaraldehyde, and periodate, Applied Biochemistry and Biotechnology, 4 (1982) 41-57.

[181] Y. Kishida, B.R. Olsen, R.A. Berg, D.J. Prockop, Two improved methods for preparing ferritin-protein conjugates for electron microscopy, The Journal of cell biology, 64 (1975) 331-339.

[182] E.I. Zenkevich, T. Blaudeck, A. Milekhin, C. Von Borczyskowski, Size-Dependent non-FRET photoluminescence quenching in nanocomposites based on semiconductor quantum dots CdSe/ZnS and functionalized porphyrin ligands, International Journal of Spectroscopy, 2012 (2011).

[183] S.T. Selvan, T.T. Tan, J.Y. Ying, Robust, Non-Cytotoxic, Silica-Coated CdSe Quantum Dots with Efficient Photoluminescence, Advanced Materials, 17 (2005)

1620-1625.

[184] B. Ekwall, Screening of toxic compounds in mammalian cell cultures, Annals of the New York Academy of Sciences, 407 (1983) 64-77.

[185] J. Pan, S.-S. Feng, Targeting and imaging cancer cells by Folate-decorated, quantum dots (QDs)- loaded nanoparticles of biodegradable polymers, Biomaterials, 30 (2009) 1176-1183.

[186] S.J. Tan, N.R. Jana, S. Gao, P.K. Patra, J.Y. Ying, Surface-Ligand-Dependent Cellular Interaction, Subcellular Localization, and Cytotoxicity of Polymer-Coated Quantum Dots, Chemistry of Materials, 22 (2010) 2239-2247.

[187] S.D. Conner, S.L. Schmid, Regulated portals of entry into the cell, Nature, 422 (2003) 37-44.

[188] I. Nabiev, S. Mitchell, A. Davies, Y. Williams, D. Kelleher, R. Moore, Y.K. Gun'ko, S. Byrne, Y.P. Rakovich, J.F. Donegan, Nonfunctionalized nanocrystals can exploit a cell's active transport machinery delivering them to specific nuclear and cytoplasmic compartments, Nano Letters, 7 (2007) 3452-3461.

[189] A. Albanese, P.S. Tang, W.C. Chan, The effect of nanoparticle size, shape, and surface chemistry on biological systems, Annual review of biomedical engineering, 14 (2012) 1-16.

[190] H. Jin, D.A. Heller, R. Sharma, M.S. Strano, Size-dependent cellular uptake and expulsion of single-walled carbon nanotubes: single particle tracking and a generic uptake model for nanoparticles, ACS Nano, 3 (2009) 149-158.

[191] M.P. Desai, V. Labhasetwar, E. Walter, R.J. Levy, G.L. Amidon, The mechanism of uptake of biodegradable microparticles in Caco-2 cells is size dependent, Pharmaceutical research, 14 (1997) 1568-1573.

[192] B.D. Chithrani, W.C. Chan, Elucidating the mechanism of cellular uptake and removal of protein-coated gold nanoparticles of different sizes and shapes, Nano letters, 7 (2007) 1542-1550.

[193] B.D. Chithrani, A.A. Ghazani, W.C. Chan, Determining the size and shape dependence of gold nanoparticle uptake into mammalian cells, Nano letters, 6 (2006) 662-668.

[194] I. Hocaoglu, F. Demir, O. Birer, A. Kiraz, C. Sevrin, C. Grandfils, H. Yagci Acar, Emission tunable, cyto/hemocompatible, near-IR-emitting Ag2S quantum dots by aqueous decomposition of DMSA, Nanoscale, 6 (2014) 11921-11931.

[195] S.J. Cho, D. Maysinger, M. Jain, B. Röder, S. Hackbarth, F.M. Winnik, Long-Term Exposure to CdTe Quantum Dots Causes Functional Impairments in Live Cells, Langmuir, 23 (2007) 1974-1980.